Magee-Womens Research Institute and Foundation

Annual Progress Report: 2012 Formula Grant

Reporting Period

July 1, 2013 – December 31, 2013

Formula Grant Overview

The Magee-Womens Research Institute and Foundation received $1,017,609 in formula funds for the grant award period January 1, 2013 through December 31, 2013. Accomplishments for the reporting period are described below.

Research Project 1: Project Title and Purpose

Maternal Lipids and Placental Function – Women with preterm births (PTB) have excess cardiovascular disease later in life, but mechanisms linking these conditions are not understood. Placental underperfusion may account for some PTBs, and perhaps mark women at risk for later life vascular disease. Incorporating placental vascular findings into studies of PTB is difficult due to nonstandard classification of what are often subtle histologic findings. Syncytial knots are groups of syncytiotrophoblast nuclei thought to reflect normal aging of the placenta at term, but excess presence in preterm placentas may indicate underperfusion. We propose to identify evidence of placental underperfusion, including excess syncytial knots in term and preterm placenta, and relate these to evidence of maternal hyperlipidemia and hypertension.

Duration of Project

1/1/2013 – 12/31/2013

Project Overview

Aims: We will utilize two data sets to study placental evidence of underperfusion in preterm births. We will evaluate 120 specimens from the Pregnancy Outcomes and Community Health (POUCH) study to achieve the following aims: 1) to validate that quantification of syncytial knots is reproducible between pathologists; 2) to identify placentas with excess syncytial knots, and relate these to evidence of maternal hypertension and hyperlipidemia. We will also link the Magee-Womens Hospital Obstetrical Maternal and Infant (MOMI) database (n=135,000) to placental pathology data to identify deliveries with pathology data, and provide preliminary data to support future studies of placental underperfusion and preterm birth.

Principal Investigator

Janet M. Catov, PhD
Assistant Professor
Magee-Womens Research Institute and Foundation and University of Pittsburgh
Magee-Womens Hospital
300 Halket Street
Pittsburgh, PA 15213

Other Participating Researchers

Claudia Holzman, PhD; Patricia Senegore, MD – employed by Michigan State University
W. Tony Parks, MD – employed by University of Pittsburgh
Karen Derzic, BA; Ye Peng, MS – employed by UPMC

Expected Research Outcomes and Benefits

Our project will validate newly proposed reference standards to distinguish normal placental maturation from pathologic evidence of underperfusion. This is an important contribution because this may make it possible to utilize placental pathology evaluations to identify subgroups of preterm birth with an underlying vascular etiology. Given that half of preterm births have unknown etiology, this can be a significant contribution that may lead to targeted interventions to reduce the prevalence of this leading cause of infant morbidity and mortality. In addition, our research will relate evidence of underperfusion in preterm birth to maternal evidence of hypertension and hyperlipidemia, and identify a possible link between preterm birth and later life maternal heart disease risk. This is important, as cardiovascular disease is the leading cause of death in women and identification of women at excess risk of cardiovascular disease can prevent or delay onset of overt clinical disease. In addition, our project will link the database of all deliveries at Magee-Womens Hospital to placental pathology data, completing an essential first step to incorporate pathology findings into population studies of preterm birth.

Summary of Research Completed

<u>Specific Aim 1</u>: To validate a quantitative approach to evaluation of syncytial knots in placentas delivered at term (≥ 37 weeks) and preterm (< 37 weeks), stratified by the presence or absence of hypertension.

During the reporting period, the research teams in Pittsburgh and Michigan continued to meet regularly to develop the protocol to quantify syncytial knots in placentas, using the published approach. The team in Michigan randomly selected 20 placental specimens for each study group (total specimens, n=160). One pathologist, Dr. Senagore, drew a grid over the central portion of one section of each specimen. This grid was comprised of ten 2 x 2 mm squares. Each pathologist then counted the number of syncytial knots in each grid square. To do so, the pathologist first centered his or her microscope field of view at 10x over the grid (Figure 1). He or she then switched to 40x for the actual counts (Figure 2). At that power, around 10 terminal villi were visible in the field.

The number of terminal villi containing at least one syncytial knot was then counted; dysmature or immature intermediate villi were counted if the terminal villi were not present. An average of 10 terminal villi were evaluated for each grid square, yielding 100 total terminal villi examined per specimen. The pathologists completed the counts using the Loukeris count. A syncytial knot was counted when it contacted another villus, but only in a minimal/partial fashion and the contour/geometry of the nuclear aggregate was such that it did not suggest a fusion of syncytiotrophoblast nuclei from an adjacent villus. The suggestion/presence of a thin clear space or nucleus-free cytoplasm between the syncytial knots and the contacting villus aided in making this decision. In addition, a "bridging" count was recorded that included the additional nuclear aggregates that fulfilled the above criteria but showed contact with another villus, suggesting there may have been fusion or syncytial "bridge" formation. The total syncytial knot count, Loukeris + bridging, was equal to or less than 10.

The average of the two individual values was used for the analysis. Inter-rater variability was evaluated using Pearson correlation coefficients. Samples of syncytial knots are shown in Figure 2.

Specific Aim 2: To identify placentas delivered, at term and preterm, with excess syncytial knots, and correlate these with clinical evidence of maternal hypertension, excess lipids, and impaired fetal growth.

The slides chosen as part of Specific Aim 1 were samples from the Pregnancy Outcomes and Community Health (POUCH) study (1998–2004), which prospectively recruited 3,019 pregnant women in mid-pregnancy from 52 clinics in five Michigan communities. The results of the counting were matched with data collected during the POUCH study. Maternal age, race, pre-pregnancy BMI, pregnancy-related hypertension, gestational age, and size at delivery were examined.

Specific Aim 3: To link deliveries at Magee-Womens Hospital with placental pathology data in order to incorporate placental data into population studies of preterm birth.

During the reporting period, we continued to analyze the deliveries with and without placental pathology data and refined the programming logic to extract key characteristics from pathology reports. We have completed the match for 21,585 delivery records from the Magee Obstetrical Maternal and Infant (MOMI) database, covering years 2008-2012.

The MOMI/Placenta database is organized by patient identification number and contains basic information, such as prenatal weight, maternal smoking status, gestational age at delivery, and birth weight. In addition, there are descriptive details of the placenta and cord and extracted information regarding types of lesions. Details on inflammatory lesions, including acute and chronic features, and non-inflammatory lesions, including a subset of non-inflammatory lesions that indicate vascular insufficiency were indicated as being present or not present in the final placenta report. This allows for reconciliation between known placenta pathologies and maternal and infant characteristics for both the validation of the approach and for the raising of new questions (see Table 1).

This new MOMI/Placenta database was then used to identify a subset of deliveries from Magee-Womens Hospital, representing term and preterm deliveries, with and without infarcts and with and without advanced villious maturation. These cases were chosen to branch both specific aims 1 and 3 of the project, by counting syncytial knots to compare to the Loukeris normal ranges. These will also be manually abstracted to validate our automated abstraction process.

The MOMI/Placenta database has already been used by a Maternal and Fetal Medicine fellow to study placental features related to pregnancy-associated plasma protein A (PAPP-A) assessed early in pregnancy. The MOMI/Placenta database was linked to the Genetics Information System. Two abstracts based on information derived from the MOMI/Placenta database were accepted for the 2014 Society of Gynecologic Investigation for poster presentations.

In addition, analysis is being completed to link with the Prenatal Exposures and Preeclampsia Prevention (PEPP3) project at Magee-Womens Hospital to compare to placenta data and with gestational weight gain and inflammatory markers.

Figure 1. 10 2x2mm squares in grid

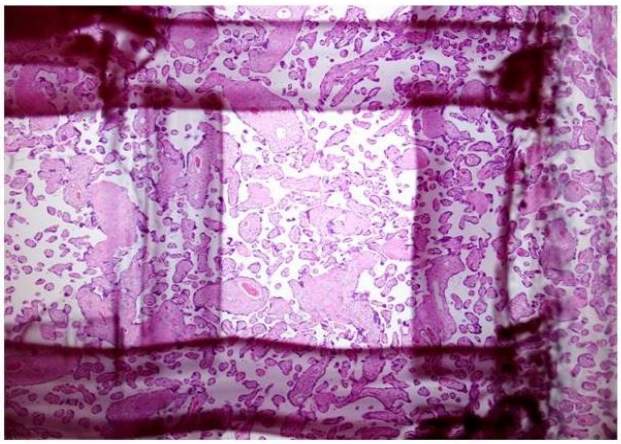

Figure 2. 40x center field

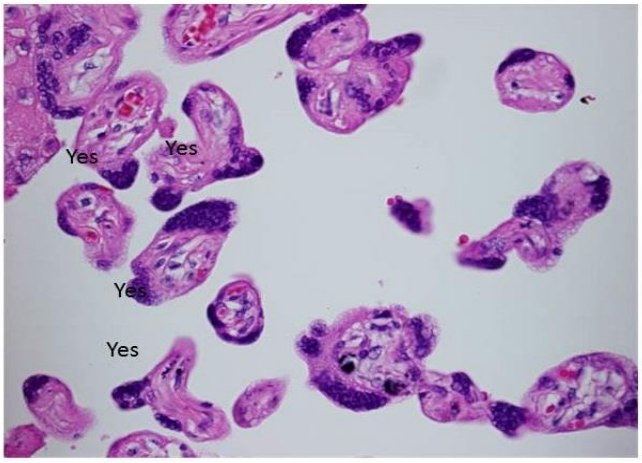

Table 1.

MOMI/Placenta Characteristics	**N=21,584**
<37 Weeks Gestational Age At Delivery	5,123
≥ 37 Weeks Gestational Age At Delivery	16,438
Race	
White	15,156
African American	4,666
Other	1,083
Smoked cigarettes during pregnancy	3,302
Pregnancy related hypertensive disorders	
Transient hypertension	1,434
Preeclampsia mild	1,749
preeclampsia severe	962
Maternal diabetes mellitus	
Type 1	1,779
Type 2	169
Gestational	58
Inflammatory Lesions	
Chorioamnionitis	7,765
Chorioamnionitis Acute	7,715
Chorioamnionitis Chronic	25
Vasculitis	3,794
Vasculitis Acute	2,718
Vasculitis Chronic	26
Deciduitis	4,364
Deciduitis Acute	3,800
Deciduitis Chronic	606
Villitis	2,771
Villitis Acute	4
Villitis Chronic	2,745
Intervillitis	39
Intervillitis Acute	3
Intervillitis Chronic	13
Phlebitis	2
Phlebitis Acute	1
Phlebitis Chronic	0
Funisitis	2,118
Funisitis Acute	2,050
Funisitis Chronic	0
Non-Inflammatory Lesions	
Chorangiomatosis	321
Perivillous Fibrin	2694

Vasculopathy	1353
Advanced Maturation	1924
Accelerated Maturation	3
Delayed Maturation	940
Thrombosis	171
Thrombotic with Cushion	346
Stromal Vascular Karyorrhexis	57
Avascular Villi	1601
Endovasculitis	39
Intraparenchymal Hemorrhages	3
Non-Inflammatory Sub-set with Vascular Insufficiency	
Subchorionic Hematomas	6
Dysmaturity	32
Syncytial Knots	1092
Distal Villous Hypoplasia	68
Villous Agglutination	79
Chorangiosis	8
Fibrin Deposition	3288

Research Project 2: Project Title and Purpose

Mouse Study of the Distribution of Placenta Originated miRNAs in the Maternal and Fetal Tissues – We hypothesize that the chromosome 19 microRNA cluster (C19MC) can be transported from the placenta into the fetus, maternal blood, and even other maternal tissues, and that the methylation status of C19MC determines its tissue-specific expression. We will use sequencing technologies to examine the expression profiles of microRNAs in a mouse model transfected with the C19MC miRNAs, apply statistical tools to interrogate the distribution and transportation of the C19MC miRNAs in the transgenic mice during pregnancy, and use the reduced representation bisulfite sequencing to investigate the methylation pattern of the C19MC region. The study may help us understand the influence of the C19MC miRNAs on human embryonic development.

Duration of Project

1/1/2013 – 12/31/2013

Project Overview

The chromosome 19 miRNA cluster (C19MC) is the largest cluster of miRNAs in the human genome. It happens that this cluster of miRNAs is also placenta specific, highly expressed in the placenta and absent in most other tissues (except for a low level expression in brain and gonads). In primary human trophoblast (PHT) cells cultured from term placenta, it was observed that the C19MC miRNAs account for about half of all miRNAs expression, and that the C19MC

miRNAs can be excreted by PHT cells, and detected in maternal blood during pregnancy.

We hypothesize that the C19MC miRNAs can be transported across the maternal-placental-fetal interfaces into fetus, maternal blood, and even other maternal tissues, and that the methylation status of CpG sites in a region close to the location of C19MC determines the tissue-specific expression of C19MC miRNAs. We will use next generation sequencing technologies to examine the expression profiles of microRNAs in a mouse model transfected with the C19MC miRNAs, obtain the expression profiles of the C19MC miRNAs in the placenta, liver, ovary, maternal plasma, and embryo of the transgenic mice, and apply statistical tools to interrogate the distribution and transportation of the C19MC miRNAs in the transgenic mice during pregnancy. We will also use the reduced representation bisulfite sequencing (RRBS) technology to examine the methylation pattern of the CpG sites close to the C19MC region, and investigate if the methylation status of these CpG sites could explain the tissue specific expression of C19MC miNRAs. Results from our data may help us to understand the influence of the C19MC miRNAs on human embryonic development, and eventually discover preventive interventions to reducing the incidence of placental related diseases.

We will achieve our goals using the experiments detailed in the following specific aims:

Aim 1: Study the transport and distribution of the human placenta specific C19MC miRNAs using a transgenic mouse model.

Aim 2: Study the methylation pattern of the genomic region around the C19MC and its relation to the expression of C19MC miRNAs in human cells and in mouse model.

Principal Investigator

Tianjiao Chu, PhD
Assistant Professor
Magee-Womens Research Institute and Foundation and University of Pittsburgh
204 Craft Ave
Room B409
Pittsburgh, PA 15213

Other Participating Researchers

Jean-Francois Mouillet, PhD; Kui Shen, PhD; Suveyda Yeniterzi, MS; Sun Huijie, BSc – employed by University of Pittsburgh

Expected Research Outcomes and Benefits

After completing this project, we will gain insight about the distribution and transportation of C19MC miRNAs during pregnancy. Specifically, the study will seek to address the following questions: 1) Are C19MC miRNAs transported from placenta to maternal blood? 2) Are C19MC miRNAs transported via maternal blood to other maternal tissues? 3) Are C19MC miRNAs natively expressed during pregnancy in maternal tissues other than brain and ovary? 4) Are

miRNAs transported from maternal tissues, via maternal blood, to placenta and fetus? Moreover, the results from this study will help us understand if the tissue specific expression of the C19MC miRNAs is primarily controlled by the methylation status of the CpG sites in the C19MC region.

Information gained from this study will help illuminate epigenomic pathways that influence human embryonic development, and suggest novel biomarkers and therapeutic approaches to obstetrical diseases stemming from placental dysfunction, which affect more than 10% of the annual four million deliveries nationwide. Moreover, the information about the epigenetic regulation of the C19MC miRNAs may help the understanding of some type of cancers, given the fact that the C19MC miRNAs are found to be expressed in certain types of aggressive brain cancers.

It is also expected that results from the proposed studies will fuel additional research and submission of new grant proposals that center on the targets and regulation of miRNAs and small RNAs in the placenta, fetal, and maternal plasma.

Summary of Research Completed

During the period from July 1 to December 31, 2013, we were mainly focusing on the study of the expression of the C19MC in various types of tissues of male transgenic mice, female non-pregnant transgenic mice, female transgenic mice, and transgenic embryos and placentas, using the mouse model we created from previous studies.

PCR data:
Using real time PCR, we measured the expression of two C19MC miRNAs that are abundant in human placenta: hsa-miR-517a-3p and hsa-miR-518b. In male transgenic mice, we found that testis has the highest miR-517a-3p expression, while kidney and liver have the lowest expression. For non-pregnant transgenic mice, brain has the highest expression, while in pregnant transgenic mice, placenta has by far the highest expression of miR-517a-3p.

To determine if pregnancy could regulate the expression of C19MC miRNAs in female organs, we transplanted wild type embryos to transgenic mice. Figure 1 shows that the expression of miR-517a-3p does not change between the non-pregnancy transgenic female mice, and the pregnant transgenic mice with only wild type embryos. This suggests that pregnancy does not change the expression of C19MC miRNAs in female organs.

We also studied the expression of C19MC miRNAs in the transgenic mouse placentas as a function of parental transgene transmission. We found that while C19MC miRNAs were always expressed in transgenic placentas, its expression in the transgenic placentas with paternally inherited C19MC BAC insert is about 3 fold of its expression in the transgenic placenta with maternally inherited C19MC BAC insert.

We compared the expression of hsa-miR-517a-3p in maternal organs of wild type females with transgenic placenta against wild type non-pregnant females. As shown in Figure 2, the miR-517a-3p expression in some tissues of wild type females with transgenic placenta seemed to be higher, but not statistically than in non-pregnant wild type female. This could be caused by

transportation of C19MC from maternal blood to maternal organs, or, alternatively, the contamination of maternal organs samples by small amount of maternal blood.

Finally, we used lentiviral transduction method to create mice expressing one of the C19MC primary miRNAs, hsa-mir-525, in the placentas, but not in the embryos. We then measured the expression of mir-525 in embryo serum, embryo brain, embryo kidney, and amniotic fluid. While the results were not all statistically significant, the higher expression observed in the wild type embryos with transgenic placenta compared to the wild type embryos with wild type placenta did suggest that C19MC expressed in the placenta could be released to embryo serum, as shown in Figure 3.

Sequencing data:

A major component of our research in the second half of the project is the sequencing of 26 miRNA libraries from samples we collected earlier, including wild type placentas from wild type mice, wild type placentas from mice also carrying transgenic placenta, transgenic placentas, brains, testes, thymuses, wild type and transgenic maternal plasma, and serum from wild type and transgenic embryos carried by the same mice.

We were able to obtained libraries with 14~40 millions of raw reads, and between 3~15 million reads aligned to mature mouse miRNA sequences (based on miRBase 20), except for the two embryo serum libraries, where we only got 0.14 and 0.37 millions of reads aligned to mouse miRNA sequences. We then aligned the reads that failed to align to mouse genome to the C19MC miRNA sequences. Summaries of these 26 miRNA libraries can be found in Tables 1a, 1b, and 2. We normalized the count of C19MC miRNAs by the total count of mouse miRNAs in each library. We found that the pattern of hsa-miR-512-5p is different from all other C19MC miRNAs, and removed it in later analysis. Figure 4 shows a clustering of the C19MC miRNA expression in the 26 libraries.

We performed Tukey's tests on the log transformed normalized total C19MC counts for each pair of types of transgenic tissues as well as the group of all wild type samples. Among the tissues we sequenced, the transgenic placenta samples have the highest C19MC expression, while transgenic liver samples do not express C19MC miRNAs. More interestingly, we found that the expression of C19MC in the wild type embryo serum from mice also carrying transgenic embryos was significantly above the wild type samples and transgenic liver samples, suggesting that C19MC miRNA could be transported from transgenic placenta, through maternal blood, to wild type embryos carried by the same pregnant mice. On the other hand, C19MC miRNAs did not express in the wild type placenta from mice also carrying transgenic embryos, suggesting that little if any C19MC miRNAs were transported from transgenic placentas via maternal blood to other placentas of the same mice.

Using Fisher's z transformation, we tested the Pearson's correlation of the log2 average expression of the top 49 C19MC miRNAs in transgenic placenta to other transgenic tissues, and found they are all significantly correlated with a positive correlation between 0.84 and 0.92. In particular, the strong correlation of the C19MC miRNA pattern in transgenic placenta and in maternal plasma with transgenic placenta suggests that C19MC miRNAs are transported not differentially, but uniformly, from placenta to maternal blood.

We also compared the mouse miRNA expression in placentas from the 3 pregnant wild type mice with transgenic dam and wild type fetuses, and 3 wild type mice with transgenic dam and transgenic fetuses. We used the normalized procedure described in the R package DESeq to calculate a size factor for each library, and performed negative binomial test with shrinkage variance estimation to test if any mouse miRNA is differentially expressed between the transgenic and wild type placentas. The p values of the tests were adjusted using the Benjamini-Hochberg's method to control the false discovery rate. We found no mouse miRNA was differentially expressed, suggesting the expression of C19MC does not affect the expression of the other miRNAs in the mouse placenta.

Methylation:

The second aim of the grant is to study the methylation pattern of the BAC transgene. We first planned a high throughput method based on next generation sequencing (Methyl-Seq) study of the BAC transgene. However, we experienced several delays due to several timed-mating that resulted in no pregnancies at all or pregnancies with no transgenic embryos. In the end we were able to obtain four pregnant transgenic mice with transgenic fetuses. Two of them were from a line with higher C19MC expression in the placenta; the other two from a line with relatively lower C19MC expression in the placenta. From each mouse we collected genomic DNA samples of 3 different tissues: placenta, ovary, and liver. We also collected two genomic DNA samples from PHTs obtained from two different placentas, one DNA sample from HTR-8 cells, and one DNA sample from U2OS cells. In total we have collected 16 DNA samples for targeted bisulfite sequencing.

Genomic DNA samples were originally isolated using QIAamp DNA mini kit (Qiagen). Unfortunately, this kit did not produce high enough yield of genomic DNA. After a few tries, we finally decided to use GenCatch Plasmid DNA Midi columns (Epoch Biolabs) in combination with Qiagen G2 lysis buffer to purify high quality genomic DNA from mouse tissues. This method allows the purification of a large amount of highly pure genomic DNA that was subsequently sheared using a Covaris focused ultrasonicator and analyzed using Agilent Bioanalyzer. At this time of writing the progress report, we have undertaken the preparation of the libraries for sequencing. We also purchased a set of Agilent SureSelectXT Custom 1kb-499 kb and SureSelectXT Methyl Reagent kit, HSQ 16, based on our custom designed probe set targeting the ~160 kb of the BAC transgene. We expect to finish the methyl-seq study by the end of February 2014.

In the absence of the targeted next generation sequencing data, we analyzed the Sanger sequencing data on bisulfite converted genomic DNA to study the methylation status of a CpG island upstream of the first miRNA gene in the BAC transgene. In the human genome this CpG island is located about 19kb upstream from the C19MC miRNAs (chr19:54,151,097-54,151,659). The sanger sequencing data consisted of 10 clones form a transgenic liver sample, 10 clones from a transgenic placenta sample with maternally inherited transgene, 7 clones from a transgenic placenta sample with paternally inherited transgene, 11 clones from a PHT cell sample, and 7 clones from a JEG3 cell sample.

Figure 5 shows the distribution of the average methylation rate over the 44 CpG sites in the sequenced CpG island for each type of tissue. We performed Wilcoxon rank sum tests to

compare the methylation rate between different types of tissues, and adjusted the test p values using Holm's method to control the family wise error rate. We found significant difference in methylation rate of the CpG island between the transgenic placenta with paternal inherited transgene and the transgenic placenta with maternally inherited transgene suggesting that imprinting of this region is maintained in the mouse genomic environment. This helps to explain the observed higher expression of the transgene in the placenta receiving the transgene from the sire than in the transgenic placenta receiving the transgene from the dam. However, the tissue specific expression of the C19MC miRNAs may be not primarily controlled by the methylation status of the CpG sites in the C19MC region, given that the transgenic placenta with maternally inherited transgene exhibited the same methylation rate as the transgenic liver, while the transgene was not expressed in transgenic liver.

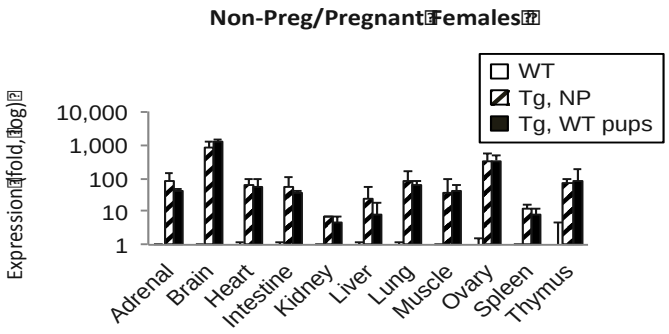

Figure 1. Expression of hsa-miR-517a-3p in pregnant and non-pregnant female transgenic mice (WT: wild type. Tg, NP: Transgenic and non-pregnant. Tg, WT pups: Trangenic, pregnant with only wild type embryos)

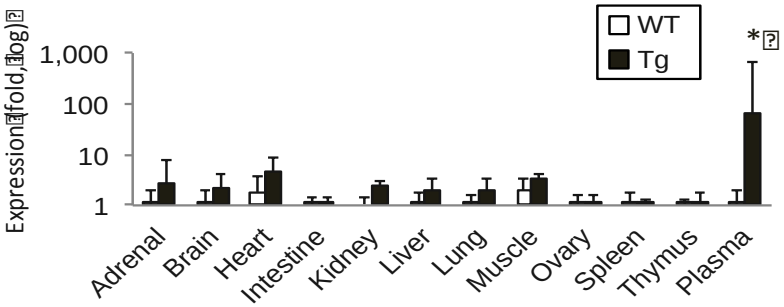

Figure 2. Expression of hsa-miR-517a-3p in maternal organs with transgenic placenta (WT: wild type. Tg: Transgenic)

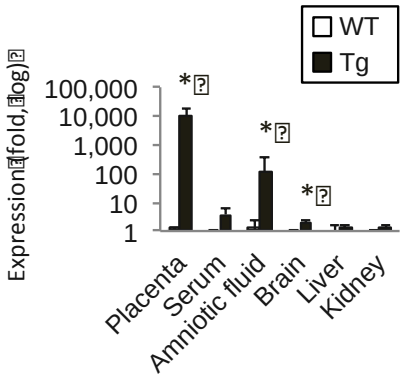

Figure 3. Expression of hsa-mir-525 in wild type fetal tissues with lentiviral transducted placenta (WT: wild type. Tg: Transgenic)

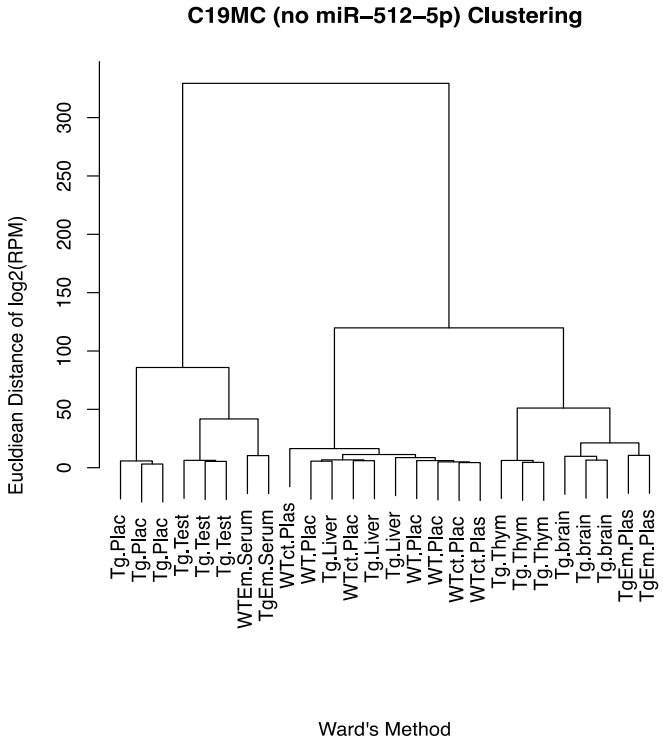

Figure 4. Clustering of C19MC miRNA in mouse miRNA libraries (For the meaning of the sample acronyms, see Tables 1a and 1b).

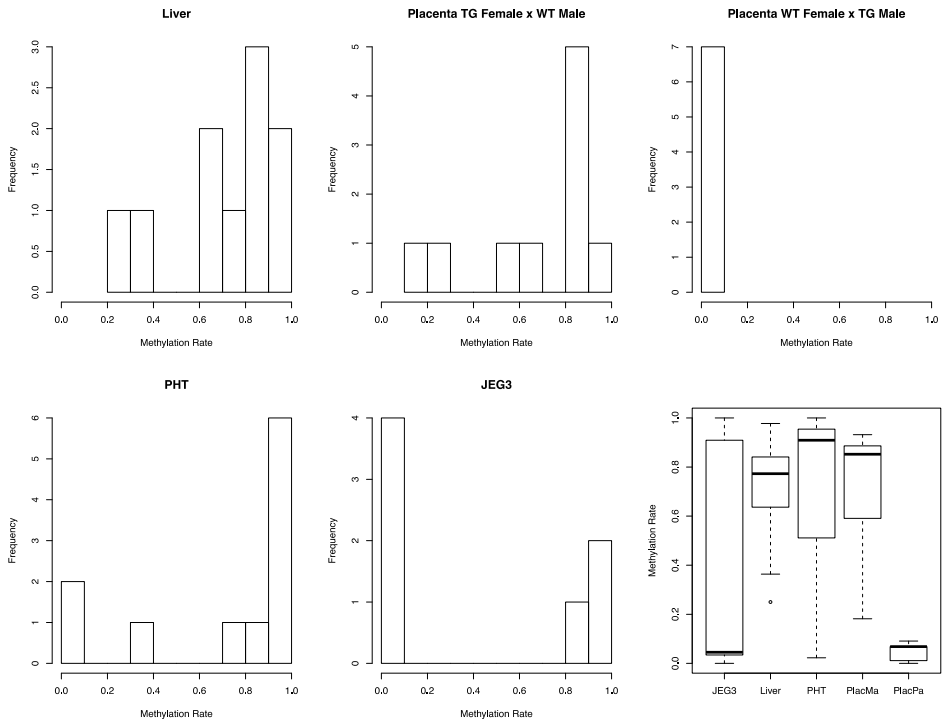

Figure 5. Methylation rate of the promoter region CGI in five tissue types (CGI: CpG island. TG: Transgenic mice. WT: Wild type mice. PHT: Primary human trophoblast cells. JEG3: Human placental choriocarcinoma cell line)

Table 1a. Placental and embryonic samples for mouse miRNA sequencing (WT: wild type. Tg: Transgenic. Note that WTEm.Serum refers to serum of wild type embryos with transgenic littermates)

Sample ID	Parents Genotype	Tissue	Tissue Genotype	Code
SL34831	WT male/WT female	Placenta	WT	WTct.Plac
SL34832	Tg male/WT female	Placenta	WT	WT.Plac
SL34833	Tg male/WT female	Placenta	WT	WT.Plac
SL34834	Tg male/WT female	Placenta	Tg	Tg.Plac
SL34841	WT male/WT female	Placenta	WT	WTct.Plac
SL34842	Tg male/WT female	Placenta	WT	WT.Plac
SL34843	Tg male/WT female	Placenta	Tg	Tg.Plac
SL34844	Tg male/WT female	Placenta	Tg	Tg.Plac
SL34852	WT male/WT female	Maternal Plasma	WT	WTct. Plas
SL34853	WT male/WT female	Maternal Plasma	WT	WTct. Plas
SL34855	Tg male/WT female	Maternal Plasma	WT mother with Tg embryos	TgEm.Plas
SL34856	Tg male/WT female	Maternal Plasma	WT mother with Tg embryos	TgEm.Plas
SL34857	Tg male/WT female	Embryo serum	WT embryos from Tg male/WT female	WTEm. Serum
SL34858	Tg male/WT female	Embryo serum	Tg embryos from Tg male/WT female	TgEM. Serum

Table 1b. Samples for mouse miRNA sequencing (WT: wild type. Tg: Transgenic)

SampleID	Mouse Genotype and Sex	Tissue	Tissue Genotype	Code
SL34835	Tg male	Brain	Tg	Tg.Brain
SL34836	Tg male	Testis	Tg	Tg.Test
SL34837	Tg male	Thymus	Tg	Tg.Thym
SL34838	Tg male	Thymus	Tg	Tg.Thym
SL34839	Tg male	Liver	Tg	Tg.Liver
SL34845	Tg male	Brain	Tg	Tg.Brain
SL34846	Tg male	Brain	Tg	Tg.Brain
SL34847	Tg male	Testis	Tg	Tg.Test
SL34848	Tg male	Testis	Tg	Tg.Test
SL34849	Tg male	Thymus	Tg	Tg.Thym
SL34850	Tg male	Liver	Tg	Tg.Liver
SL34851	Tg male	Liver	Tg	Tg.Liver

Table 2. Summaries of mouse miRNA sequencing libraries

SampleID	lib.size	mm.miRNA	c19mc (no miR-512)	c19mc.rpm
SL34831	30069683	10494728	279	26.58477666
SL34832	21229160	7874721	72	9.143181073
SL34833	28897441	10720060	135	12.5932131
SL34834	24500232	9191095	421151	45821.63496
SL34835	32452042	15335917	4882	318.3376645
SL34836	31627989	4162657	28795	6917.456807
SL34837	20340882	8677899	8805	1014.646518
SL34838	20625957	8593973	13035	1516.760641
SL34839	39698382	15559593	107	6.876786559
SL34841	23217495	9971683	74	7.421014086
SL34842	23073000	10269803	90	8.763556614
SL34843	19418846	8849501	449229	50763.20122
SL34844	14388654	6578608	402635	61203.67713
SL34845	22623671	12282904	1454	118.375915
SL34846	17823988	9761669	1760	180.2970373
SL34847	20688438	3769293	25036	6642.094419
SL34848	19856178	3903576	21267	5448.081451
SL34849	15199500	7233628	5914	817.570381
SL34850	22434974	8791969	160	18.19842631
SL34851	18843361	7581122	96	12.66303326
SL34852	27081836	5730288	276	48.1651184
SL34853	24888872	10663780	112	10.50284233
SL34855	25102843	8424037	1644	195.155838
SL34856	24598140	9116152	3233	354.6452494
SL34857	32443273	146551	50	341.1781564
SL34858	33775433	370401	186	502.1584715

Research Project 3: Project Title and Purpose

Preeclampsia and Post-partum Vascular Function – This project is designed to learn more about the relationship of the pregnancy complication preeclampsia (PE) and blood vessel function after pregnancy. PE affects about 5% of all pregnant women, and these women are more likely to get cardiovascular disease (CVD) years after pregnancy. We believe that measureable deficiencies in vascular function in young women after a PE pregnancy are surrogate markers of future CVD. This project to measure carotid-femoral pulse wave velocity (vessel stiffness) and brachial artery flow-mediated vasodilation, and their relationship to sublingual artery surface layer (glycocalyx) depth and circulating lipids, could help clarify why CVD risk is increased in women who have

had PE.

Duration of Project

1/1/2013 – 12/31/2013

Project Overview

Compared to women who had normal (uncomplicated) pregnancies, women who experienced preeclampsia (PE) in a pregnancy are at heightened (2- to 8-fold) risk of cardiovascular disease (CVD; hypertension, stroke, ischemic heart disease) in later life. The reasons for this remain unclear. Vascular stiffness (pulse wave velocity; PWV) and endothelium-dependent responsiveness of the brachial artery to an increase in shear stress (flow-mediated vasodilation; FMD) are indirect (surrogate) measures of later life CVD risk in both healthy and diseased populations. In the postpartum state, FMD may be diminished in women with prior PE compared to women with prior normal pregnancy. However, available data were obtained using flawed approaches. We will test how these vascular function variables, measured using current guidelines, are related to status of the protective matrix that coats blood vessels (glycocalyx; GCX) by also measuring (a) urinary podocalyxin (a measure of renal podocyte GCX dysfunction) and (b) GCX width/integrity in microvessels of the tongue. We will study 18 non-pregnant women with a history of PE compared to 18 non-pregnant women with a history of normal pregnancy, 6 to 48 months after first pregnancy.

Aim 1. To test the hypothesis that brachial artery FMD is reduced and brachial-radial artery PWV is increased (adverse changes) in women with prior PE, compared to women with prior normal pregnancy, and determine whether the shear stimulus and the time to peak FMD are altered among women with prior PE.
Aim 2. To compare groups regarding sublingual capillary and venular GCX structural integrity and sublingual capillary density by sidestream dark field imaging. Compare maternal urinary podocalyxin as an indicator of renal glycocalyx damage/turnover.
Aim 3. To determine the relationship between vascular dysfunction, glycocalyx variables and circulating bioactive lipids potentially implicated in GCX damage.

The project will help clarify relationships between previous PE and vascular function in different tissue beds. The project will also provide data to facilitate NIH funding and our long-term goal of developing effective assessments and interventions for CVD in women according to pregnancy profile and history.

Principal Investigator

Carl A. Hubel, PhD
Associate Professor
Magee-Womens Research Institute and University of Pittsburgh
204 Craft Avenue
Pittsburgh, PA 15213

Other Participating Researchers

Robin E. Gandley, PhD; Arundhathi Jeyabalan, MD – employed by Magee-Womens Research Institute and University of Pittsburgh
Judith Brands, PhD – employed by University of Pittsburgh
Tracey L. Weissgerber, PhD – employed by Mayo Clinic, Rochester, MN

Expected Research Outcomes and Benefits

The etiology and pathogenesis of the multi-system pregnancy disorder preeclampsia (PE), and the reasons why women with a history of PE are at increased risk of future cardiovascular disease (CVD) remain poorly understood. Although PE itself may have lasting adverse effects, we believe that PE is primarily a harbinger/surrogate marker of heightened CVD risk. In any case, there are significant gaps in our understanding of deficiencies in vascular function that may exist in women after a PE pregnancy. The vascular endothelial GCX is a coating on the external (apical) cell surface that is critical to healthy vascular function. Our previous research showed significant disturbances in placental syncytiotrophoblast GCX composition. We propose, as a logical extension, to test whether maternal microvascular GCX damage correlates with peripheral arterial endothelial dysfunction and atherogenic lipids in women with prior PE compared to women with prior normal pregnancy, in the non-pregnant state 1 year after pregnancy (n=18 per group). In collaboration with researchers at the University of Pittsburgh Center for Ultrasound Molecular Imaging and Therapeutics, we will use non-invasive sidestream dark field (SDF) imaging to enable real-time intravital observation of the sublingual microcirculation. We will use SDF to quantify sublingual capillary density and capillary/venular glycocalyx (GCX) width/integrity and examine the relationship of these variables to measures of peripheral vascular function. Although this is not a clinical trial and may not have immediate translation to patient care, this project will advance our understanding of the pathogenesis of PE and its link to future CVD, and may lead to therapeutic avenues.

Summary of Research Completed

Substantial progress has been made toward completion of all of the Aims.

The methods described in this report were by design used both during the reporting period, January 1, 2013 – June 30, 2013 and July 1, 2013 – December 31, 2013. The methods reported were planned as part of the original research proposal for Aims 1-3. The research involved patient recruitment over the span of January 1, 2013-December 31, 2013.

<u>Specific Aim1, Study participant (patient) enrollment</u>:
During the first 6-month reporting period (January 1, 2013- June 30, 2013), 11 postpartum women were enrolled into the study performed at the Clinical and Translational Research Center (CTRC) at Magee-Womens Hospital. Of these 11 however, one was deemed to have proteinuria without gestational hypertension, and one had gestational hypertension but did not develop proteinuria. Therefore, these two individuals did not meet criteria for either the preeclampsia or uncomplicated (control) pregnancy study groups. During the second 6 months <u>(July 1, 2013 – December 31, 2013)</u>, 6 additional postpartum women were enrolled into the study performed at

the CTRC. All 6 of these women met pregnancy outcome criteria. The total current case-control comparison study groups over the period January 1, 2013-December 31, 2013, thus consist of n=9 postpartum women with a history of uncomplicated pregnancy and n=6 postpartum women with a history of preeclampsia.

An additional 19 eligible women were identified; of these, 15 either did not reply to our contact or were unable to be contacted. Three patients had another pregnancy and were thus ineligible on that basis. One patient reported being unable to get sufficient time off from work.

We are endeavoring to continue recruitment to increase the study sample size. Although we received a percentile score of 12.0, the Preeclampsia Program Project (PI: Hubel, CA) was not renewed by NIH. We were not able to support our recruiting staff after October 31, 2013. We trained our remaining laboratory technicians (at Magee-Womens Research Institute) to perform the tasks of patient contact, recruiting, and scheduling. The study lost 2 months of recruitment time in the process. There are currently three newly identified postpartum women who have agreed to participate in the study and are scheduled to the CTRC for vascular tests in March 2014.

Aim 1 Vascular Assessment Methods:
Hemodynamic data: The ejection of blood from the ventricle into the aorta generates an aortic pressure pulse. There is often a systolic shoulder on the ascending limb pressure curve coinciding with peak flow, followed by a rise in pressure to the systolic peak. This second increase in pressure is the augmentation pressure (AP) and is primarily due to the reflected components of the original pressure pulse generated by ventricular ejection. AP is the pressure difference between the first peak/shoulder and the second peak/shoulder. The amount of augmentation increases as the arteries stiffen. The augmentation index (AI) is the AP divided by the central pulse pressure. AI and AP are best compared when normalized to a fixed heart rate. Calculated variables thus included aortic systolic and diastolic blood pressure, aortic pulse pressure, mean arterial pressure, AI, AP, AI normalized to a fixed heart rate of 75 beats per minute, and AP normalized to a fixed heart rate of 75 beats per minute (Table 1).

Pulse wave velocity (PWV): Carotid-to-fermoral PWV, an index of vascular stiffness) was analyzed off-line by a custom-developed MATLAB program.

Flow-mediated vasodilation (FMD): Continuous brachial artery images in the dominant arm were obtained using a 10 MHz probe operating in B-Mode (GE Vivid i system). Blood velocity was simultaneously recorded by Doppler ultrasound, with the same probe operating at 4 MHz and an insonation angle <60°. The occlusion cuff was positioned on the forearm. The probe was proximal to the cuff. Simultaneous diameter and blood flow velocity images were obtained for 1 minute of baseline, 5 minutes of occlusion (cuff inflation to 200 mmHg), and 5 minutes post-release. Images were recorded continuously, using a digital capture system). Calculated values included: FMD; the shear stimulus for FMD (shear stress area under the curve from cuff release to the time of peak diameter); and low flow-mediated constriction (L-FMC). L-FMC is a measurement of vessel constriction above the blood pressure cuff. L-FMC occurs in some patient populations during occlusion and is postulated to be a response to reduced shear.

Aim 1 Vascular Assessment Results:
The central hemodynamic data and pulse wave velocity-related data accumulated during the reporting period are presented in Table 1. During the previous reporting period there were two patients (one postpartum woman with prior preeclampsia, and one postpartum women with prior uncomplicated pregnancy) who had completed the study but whose data had not been analyzed. Therefore, during the current reporting period we analyzed hemodynamic data from six women with prior uncomplicated pregnancy and two with prior preeclampsia.

Flow-mediated vasodilation: The material transfer agreement between the University of Pittsburgh and the Mayo Clinic was completed in September 2013, allowing our collaborator, Tracey Weissgerber (now Assistant Professor at the Mayo Clinic) to analyze these data. Brachial and radial artery FMD data were successfully collected on all but one study participant. However, not all data were of analyzable quality, a problem primarily with women of BMI >30. Table 2 lists, by patient group, the overall current results and sample size for each measured variable. The current data (Table 2) suggest that brachial and radial FMD do not differ between women with a history of preeclampsia and women with a history of uncomplicated pregnancy, 1 year postpartum. However, we have not yet achieved the sample size (15/group) estimated as necessary to detect a significant difference. Substantial discrepancies in FMD protocols exist across different laboratories, and there is also wide inter-subject variability in hyperemic shear stress (the stimulus for FMD). One can normalize the measured vasodilation response to the applied stimulus; in other words, dividing the peak FMD by the shear stress area under the curve (individual area until peak FMD). To date, however, no differences in shear rate area under the curve have been observed (Table 2). The degree of radial artery vasoconstriction during reduced flow caused by wrist occlusion (low flow-mediated constriction, L-FMC) was recently proposed as a vascular function test. Mean radial artery L-FMC in healthy subjects is 2 to 7%, and radial L-FMC may be diminished in hypertensive patients compared with healthy subjects. We *hypothesized that*, compared to women with a previous uncomplicated pregnancy, radial artery, but not brachial artery, L-FMC will be diminished among postpartum women with previous preeclampsia. Although with limited sample size to date, this hypothesis does not appear to be supported (Table 2).

Aim 2 Methods:
Imaging of the sublingual microvasculature was performed (during this reporting period, July 1, 2013 – December 31, 2013) on six women with prior uncomplicated pregnancy and one woman with prior preeclampsia.

Aim 2 Results:
The data accumulated during the second reporting period (July 1, 2013 – December 31, 2013) (six women with prior uncomplicated pregnancy and one woman with prior preeclampsia) are given in Table 3. The data presented in Table 3 supplement data collected in the previous reporting period. The collection of this data was part of the original research proposal. Milestones for analyses were met but patient recruitment goals were not met (see also Aim 1 Results).

Aim 3 Methods:
Maternal plasma total triglycerides, total cholesterol and total free (non-esterified) fatty acids

were measured both at 20 weeks of gestation and in samples obtained at the 1-year postpartum CTRC visit. Free fatty acids were quantitatively determined by an enzymatic, colorimetric method developed by Wako Pure Chemical Industries, Ltd. Coefficient of variation between runs was 6.5%. Cholesterol and triglycerides were measured in duplicate by colorimetric techniques, using commercial kits from Pointe Scientific (Canton, MI); the average coefficients of variation between runs ranged from 5.3 percent to 8.4 percent.

Mid-pregnancy maternal plasma samples were available (mean gestational age, 20 weeks; range, 15-23 weeks). This time period was at least 4 weeks before clinically evident preeclampsia. With the exception of mid-pregnancy lipid measurements, all of the research activities described in this section were originally planned in the research proposal. The lipid measurements at mid-pregnancy (20 weeks') were performed after we realized that the plasma samples were available. The purpose of this deviation from the original research proposal was to see if pregnancy lipids correlate with vascular function measures in the post-partum state.

Aim 3 Results:

Mid-pregnancy plasma triglycerides, but not cholesterol or total free (non-esterified) fatty acid, concentrations were significantly higher in the group of women who subsequently developed preeclampsia (Table 4). Cholesterol and triglyceride values were not significantly different between the groups 6-24 months after pregnancy (Table 4). We have purchased an additional kit for free fatty acid measurements, which have not yet been completed. The performance of these analyses partially met the milestones for Aim 3. The urinary podocalyxin measurements and measurement of plasma sphingolipids have not yet been carried out. These analyses will be done in batch (to avoid inter-assay variability) after recruitment has ended. Only at that point can the tests of correlation with vascular variables be completed.

Table 1. Central hemodynamic and pulse wave velocity data Table 1. Central Hemodynamic and Pulse Wave Velocity Data

Pt #	Pregnancy Outcome	Radial artery systolic blood pressure	Radial artery diastolic blood pressure	Radial artery pulse pressure	Systolic blood pressure	Diastolic blood pressure	Aortic pulse pressure	Mean arterial blood pressure	Heart rate (bpm)	Augm. Index	Augm. pressure	Aortic AI 75	Aortic AP 75	PWV carotid femoral
11	Control	110.0	62.0	48.0	94.0	63.0	31.0	76.0	60.0	10.5	3.5	3.5	1.0	
13	Control	108.0	66.0	42.0	96.0	67.0	29.0	80.0	62.0	15.4	4.6	9.2	2.6	4.23
14	Control	93.0	54.0	39.0	82.0	55.0	28.0	67.0	74.0	17.5	5.0	17.0	4.8	3.97
15	Control	98.0	68.0	30.0	85.5	68.75	16.75	76.0	83.5	-15.25	-2.75	-11.25	-1.75	4.00
16	Control	125.0	79.0	46.0	116.0	79.7	36.3	95.7	58.0	26.7	9.7	18.0	5.7	5.97
17	Control	99.0	59.0	40.0	86.0	60.0	26.0	72.3	74.8	10.8	2.8	10.8	2.8	
All controls: Group Mean		105.5	64.7	40.8	93.2	65.5	27.6	77.9	68.6	10.9	3.8	7.9	2.5	4.5
Std Dev:		11.5	8.6	6.3	12.3	8.6	6.4	9.7	10.2	14.1	4.0	10.8	2.7	1.0
2	PE	118.0	61.0	57.0	105.0	62.0	43.0	81.0	53.0	22.3	9.3	12.0		3.03
10	PE	132.0	97.0	35.0	126.0	98.0	28.0	112.0	61.0	29.0	8.0	22.0	5.5	6.10
All PE's: Group Mean		125.0	79.0	46.0	115.3	79.8	35.5	96.4	56.9	25.7	8.7	17.0	5.5	4.6
Std Dev:		9.9	25.5	15.6	15.1	25.7	10.6	21.3	5.1	4.7	0.9	7.1		2.2

Table 1 Legend: Aortic AI 75: Augmentation (Augm) index normalized to a fixed heart rate of 75 beats per minute (bpm); Aortic AP 75: Augmentation pressure normalized to a fixed heart rate of 75 beats per minute. PWV: Pulse wave velocity

Table 2: FMD-related data

Brachial artery data	Prior uncomplicated pregnancy	Prior preeclampsia	P value
Brachial baseline diameter (mm)	3.1±0.12 (n=7)	3.2±0.57 (n=4)	NS
Shear rate area under the curve, brachial artery	20290±9898 (n=7)	18809±7542 (n=4)	NS
Brachial flow-mediated dilation (FMD) (%)	7.58±4.06 (n=7)	6.87±2.68 (n=4)	NS
Brachial low flow-mediated constriction (L-FMC) (%)	-0.16±1.2 (n=7)	0.89±0.29 (n=4)	NS
Radial Artery Data			
Radial baseline diameter (mm)	1.95±0.22 (n=5)	2.22±0.042 (n=3)	NS
Shear rate area under the curve, radial artery	18388±6483 (n=5)	20016±10245 (n=3)	NS
Radial flow-mediated dilation (FMD) (%)	5.30±2.75 (n=5)	6.53±3.26 (n=3)	NS
Radial low flow-mediated constriction (L-FMC) (%)	-1.50±3.08 (n=5)	-2.27±0.12 (n=3)	NS

Patient #	Pregnancy Outcome		Red blood cell filling percentage	PBR averaged across the major range of vessel sizes (5-25 microns)
11	Control		66.4	8.58
13	Control		77.7	10.01
14	Control		71.4	9.71
15	Control		70.9	11.55
16	Control		76.8	10.08
17	Control		77.4	11.30
	all controls:	Group Mean	73.4	10.2
		std dev:	4.6	1.1
2	PE		58.3	12.71

Table 3: *Red blood cell filling percentage*. Red blood cell (RBC) filling is reduced (greater percentage of microvessel segments lacking red cells) in poorly perfused microvessels. Perfused boundary region (*PBR) values*, classified according to their corresponding RBC column width values (between 5 and 25 µm), are averaged to provide a single average PBR value for each patient. Glycocalyx damage increases the PBR of the glycocalyx. Preeclampsia (PE): history of preeclampsia. Control: history of uncomplicated pregnancy.

Table 4. Mid-gestational and 6-24 month postpartum lipids, Uncomplicated Pregnancy and Preeclampsia Groups

	Uncomplicated Pregnancy (n=9)	Preeclampsia (n=5)	P value
Gestational age at venipuncture (mid-pregnancy blood sample) (weeks)	20.3 ± 1.3	19.0 ± 3.2	NS
Mid-pregnancy cholesterol (mg/dL)	202 (175-220)	180 (164-263)	NS
Mid-pregnancy triglyceride (mg/dL)	102 (76-109)	136 (108-171)	P<0.05
Mid-pregnancy free fatty acids (mmol/L)	0.31 (0.15-0.41)	0.23 (0.17-0.33)	NS
Postpartum Cholesterol (mg/dL)	105 (77-139)	132 (88-148)	NS
Postpartum Triglyceride (mg/dL)	48 (37-62)	40 (28-64)	NS

Research Project 4: Project Title and Purpose

Oxidative Stress, Hypoxia and Placental Cholesterol Metabolism – While oxidative stress and hypoxia are known to cause placental injury and to disrupt cholesterol homeostasis, their effect on placental cholesterol metabolism is not known. We posit that disruption of placental cholesterol homeostasis adversely affects placental function and fetal growth. Our focused interrogation of placental cholesterol metabolism and its effect on fetal growth will elucidate central pathways in placental metabolic function, and highlight therapeutic targets for the amelioration of placental injury.

Duration of Project

1/1/2013 – 12/31/2013

Project Overview

Fetal growth and development are dependent on the placenta, which mediates nutrient and gas exchange, removal of waste products, immunological protection of the allogeneic fetus, and pregnancy-specific endocrine signaling. Placental injury and subsequent dysfunction lead to fetal growth restriction (FGR), and confer risk for perinatal death, neonatal morbidity, neurodevelopmental disorders, and adult disease. Despite the associated risks, a large knowledge gap persists regarding the pathobiology of placental dysfunction and FGR. The only therapeutic option for women with pregnancies affected by FGR is delivery, often compounding underlying pathology with the sequelae of iatrogenic prematurity.

Cholesterol is essential for the integrity of cellular membranes, and plays a pivotal role in multifold synthetic and signaling pathways. Cholesterol homeostasis can be disrupted by oxidative stress or hypoxia, and limited prenatal cholesterol availability is associated with

impaired fetal growth and developmental abnormalities. Whereas hypoperfusion and the resultant hypoxia are common causes of placental injury, the impact of oxidative stress and hypoxic injury on placental cholesterol metabolism, and the subsequent effect on placental function and fetal growth, remain unknown.

As a part of our long-range goal of elucidating pathways that define trophoblast dysfunction, we seek to test the hypothesis that hypoxia and oxidative stress disrupt placental cholesterol trafficking and metabolism, leading to impaired trophoblast function and restriction of fetal growth. We will test this hypothesis using the following Aims:

Aim 1 - Decipher the regulation of placental cholesterol homeostasis, and determine the effect of hypoxia and/or oxidative stress on placental cholesterol processing and oxidation.

Aim 2 - Determine the effect of hypoxia and oxidative stress on expression of transcriptional regulators and effectors of cholesterol metabolism.

Principal Investigator

Jacob C Larkin, MD
Visiting Assistant Professor
Magee-Womens Research Institute and Foundation and University of Pittsburgh
Magee-Womens Hospital
300 Halket St.
Room 2229
Pittsburgh, PA 15213

Other Participating Researchers

Robert W. Powers, PhD – employed by University of Pittsburgh

Expected Research Outcomes and Benefits

Intracellular concentrations of cholesterol and its metabolites regulate ligand-binding and activation of multiple sterol-responsive transcription factors. Thus, the potential sequelae of aberrant regulation of sterol metabolism are far-reaching. We posit that disruption of placental cholesterol homeostasis could adversely impact fetal growth via the following mechanisms:

1. Reduced maternal to fetal cholesterol transport.
2. Sterol-induced cytotoxicity causing placental cell death and compromise of function.

Cholesterol is a vital determinant of multiple diverse biological pathways, and a critical substrate for growth. The importance of maternal-fetal cholesterol transport for normal fetal development has been definitively established, highlighting the need for novel insights into cholesterol trafficking between mother, placenta and fetus. Nonetheless, the regulation of placental cholesterol metabolism and its impact on placental function and fetal growth remain largely unknown. In the proposed studies, we will interrogate the role of placental cholesterol homeostasis in placental biology with a focus on the mechanisms of action detailed above. We

will complement experiments in primary human trophoblasts with analysis of human specimens and *in vivo* studies of pregnancy in mice. Our work will decipher critical components of prenatal metabolic regulation and is likely to illuminate the pathophysiology of fetal growth restriction that stems from placental metabolic injury in an unprecedented manner.

Summary of Research Completed

From July 1, 2013 – December 31, 2013, we have made further significant progress toward achieving our stated aims, as outlined below:

Aim 1:
We have published data demonstrating the effect of intrauterine hypoxia on the expression of several lipoproteins implicated in lipid transport within the placental labyrinth (Larkin, et al., *Endocrinology* 2014; en20131425 [Epub ahead of print], and acknowledged the Pennsylvania DOH as a funding source. We have also performed a series of experiments, as outlined in our initial research proposal, using primary human trophoblasts (PHT), to determine the effect of hypoxic exposure on progesterone synthesis. Cells were initially plated at standard oxygen tension (21% O_2) in standard medium with 10% fetal bovine serum. 24 hours after plating, cells either remained at standard O_2 tension (21% O_2), or were transferred to an 8% or <1% O_2 environment. All medium was replaced with serum-free medium at 24 hours after plating. As shown in Figure 1, environmental O_2 levels significantly impact progesterone secretion in trophoblasts, with declining secretion at lower O_2 levels. Cells were treated with increasing doses of free cholesterol, low-density lipoprotein (LDL), or 25-hydroxycholesterol (25OHC), a product of cholesterol oxidation (Fig. 2). Consistent with the findings shown in Figure 1, progesterone secretion was dramatically reduced in hypoxia. Furthermore, when exposed to O_2 tension below 1%, PHT cells demonstrated increased progesterone secretion with increasing substrate availability ($p<0.05$, test for trend for all substrates), while at 8% O_2, substrate availability had a variable effect on progesterone secretion, with no significant trend detected.

Aim 2:
In addition to the work performed under Aim 1, we uncovered novel findings in pursuit of Aim 2. This work was directly supported by Pennsylvania DOH funding. As demonstrated in Figure 3, both 25OHC and the liver X receptor (LXR)-specific ligand T0901317 induce cell toxicity in a dose-responsive fashion. Similarly, both T0901317 and 25OHC inhibit trophoblast differentiation as determined by hCG secretion (see manuscript 'The influence of ligand-activated LXR on primary human trophoblasts' listed under Item #20 of the Final Progress Report). However, at 21% O_2, T0901317 elicits a dose-dependent reduction in progesterone secretion, while 25OHC has a variable effect on progesterone secretion at differing doses, with no discernable monotonic trend (Fig. 4). We also observed a discrepant effect of the two LXR ligands on lipid droplet formation. T0901317 (10 μM) and hypoxia (FiO_2<1%) provoked robust lipid droplet formation, while 10 μg/mL 25OHC had no detectable effect on lipid droplet formation (Fig. 4). To identify changes in gene expression that underlie the discrepant cellular effects of LXR ligands in human trophoblasts, we compared changes in gene expression elicited by these ligands. As shown in Fig. 5, while T0901317 had no effect on expression of the Sterol-Response Element Binding Protein 2 (SREBP2) target LDL receptor (LDLR), exposure of PHT cells to T0901317 led to increased expression of ABCA1, SREBP1c, ACC1, and FAS. Similar

to the effect of T0901317, exposure to 10 μg/mL of 25OHC did not significantly impact expression of SREBP2, or LXRβ, and led to an insignificant increase in expression of LXRα. However, unlike T0901317, 25OHC selectively upregulated specific LXR targets, causing increased expression of the cholesterol efflux mediator ABCA1, with no effect on the expression of the lipogenic genes SREBP1c, ACC1, or FAS. Additionally, 25OHC inhibited expression of LDLR. These findings indicate that not only does LXR activation influence specific trophoblast functions, but that it does so in a ligand-specific manner. The discrepancy in the functional and transcriptional effect of the two studied LXR ligands suggests that LXR is a potential therapeutic that can be targeted with selective ligands to activate specific targets and cell functions.

Figure 1– Effect of ambient oxygen and substrate concentration on progesterone secretion. PHT cells were treated with the indicated dose of free cholesterol, LDL, or 25OHC and indicated O_2 tension. Progesterone concentration in cell media was measured 72 hours after plating.

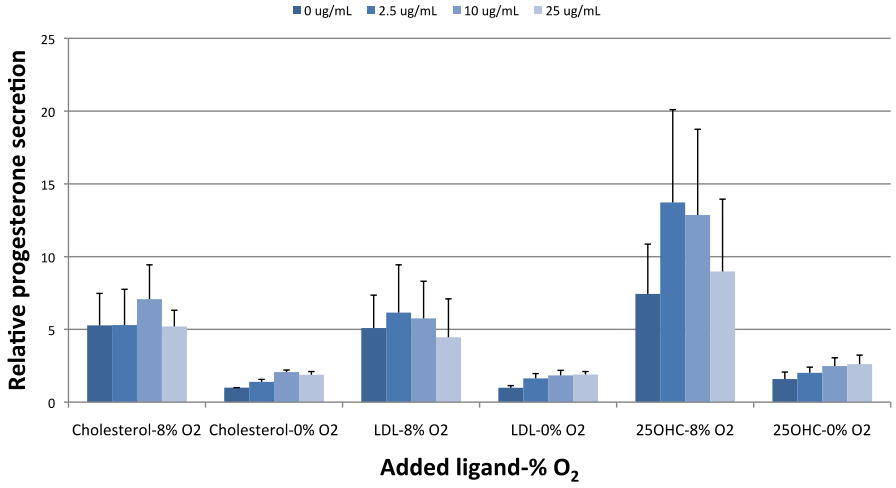

For all figures, PHT=primary human trophoblast cells, 25OHC= 25-hydroxy cholesterol, hCG=human chorionic gonadotropin, LDH=lactate dehydrogenase, LDL=low-density lipoprotein, ApoA1=ApolipoproteinA1, HDL=high-density lipoprotein, SREBP=Sterol Response Element Binding Protein, LXR=Liver X Receptor, LDLR=LDL receptor, ABCA1=ATP Binding Cassette Transporter A1, ACC1=Acetyl-CoA carboxylase, FAS=Fatty Acid Synthase, RT-qPCR=reverse transcriptase quantitative PCR.

Figure 2 – LXR ligands cause trophoblast toxicity. PHT cells (n=3) were treated with the indicated dose of T0901317 or 25OHC 24 h after plating. LDH levels were measured 48 and 72 h after plating. The non-parametric test of trend for LDH release was significant with increasing doses of both ligands at both time points ($p<0.005$).

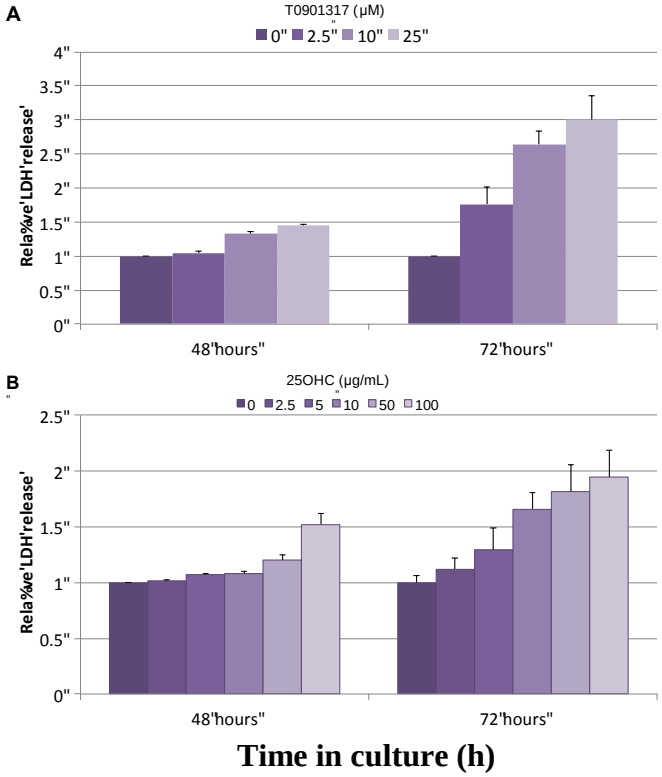

Figure 3 – Effects of 25OHC and T0901317 on progesterone secretion. PHT cells were cultured at 21% O_2 and treated with the indicated dose of 25OHC or T0901317 24 h after plating. Progesterone concentration in cell medium was measured 72 h after plating.

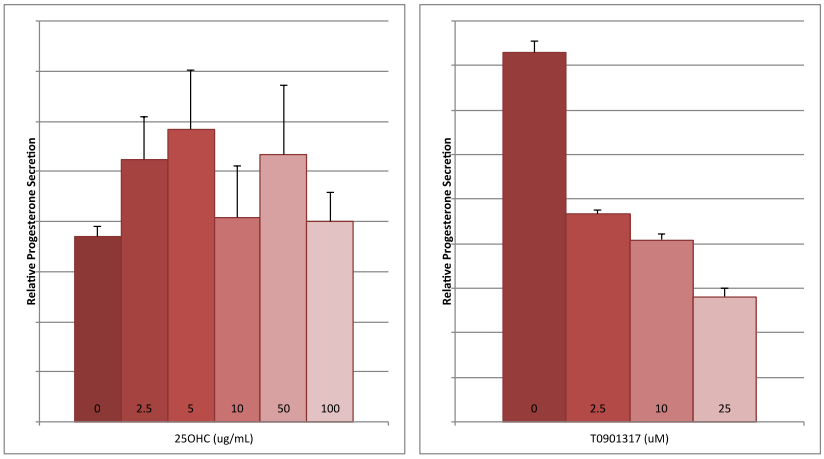

Figure 4 – Effect of LXR ligands on lipid droplet formation . PHT cells were exposed to vehicle only, FiO_2<1%, 10 µM T0901317, or 10 µg/mL 25OHC prior to fixation and staining. Lipid droplets are stained with green BODIPY dye.

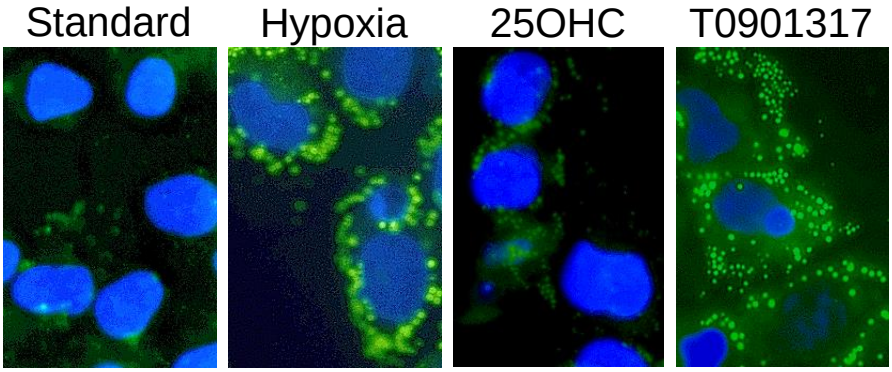

Figure 5 – Effect of LXR ligands on gene expression in human trophoblasts. RT-qPCR results (n=3, all experiments). *p<0.05 by Student's two-tailed t-test compared to cells exposed to vehicle only.

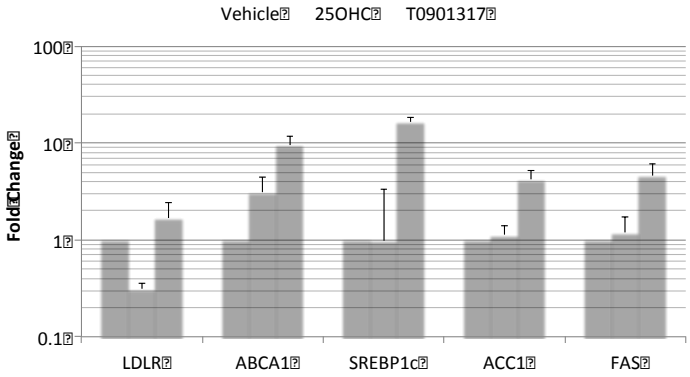

.

Research Project 5: Project Title and Purpose

Effects of Telomerase Inhibitors on Centrosomes and Centromeres in Cancer Cells – Nearly all human cancers bypass replicative senescence and DNA damage signaling pathways by preventing the shortening of telomeres, the protective 'caps' at chromosomal ends, using the reverse transcriptase Telomerase. This cancer cell exclusive enzyme is an ideal biomarker and target for cancer diagnosis, prognosis and therapies. Genomic instabilities also correlate with centrosomal abnormalities and defects to the spindle assembly checkpoint (SAC) system, increasing spindle multipolarity and chromosome misalignment, a hallmark of many cancers. Here, fixed and dynamic confocal imaging with living markers for centrioles and microtubules are used to explore the telomerase inhibitors impact on centrosome and SAC constituents in normal somatic and cancerous cells.

Duration of Project

1/1/2013 – 12/31/2013

Project Overview

This project explores whether telomerase inhibitors interfere with centrosome function and duplication as well as protein constituents of the spindle assembly checkpoint (centromeres) in normal as well as lung and breast cancer cells. The two specific aims are:

Aim I. What are the effects of Telomerase Inhibitors (TIs) on cancer cell viability, DNA synthesis, metabolic activity, and Telomerase activity?
Question 1. Do TIs impact growth and proliferation of control WI-38 and NCI H292 or MCF7 cancer cells?
Question 2. Do TIs impact DNA synthesis in a dose-dependent manner in control WI-38 and NCI H292 or MCF7 cancer cells?
Question 3. What are the effects of TIs on the metabolic activity of control WI-38 and NCI H292 or MCF7 cancer cells?
Question 4. Do TIs inhibit endogenous telomerase activity in a dose-dependent manner in control WI-38 and NCI H292 or MCF7 cancer cells?

Aim 2. At the maximum effective dose of TI, which inhibits cell growth and proliferation of cancer cells as determined in Aim 1, what are the effects of telomerase inhibition on centrosome and centromere function in control WI-38 and NCI H292 or MCF7 cancer cells?
Question 1. Do TIs impact microtubule (mt) organization from the centrosome and do they affect mt dynamics following drug induced disassembly or rescue from mt depolymerization?
Question 2. Do TIs block centrosome duplication in a dose-dependent manner?
Question 3. Do TIs block cell cycle progression in a dose dependent manner?
Question 4. How do TIs impact proteins involve in centromere assembly and the spindle checkpoint pathway during mitosis*?*

Methods employed include the use of fixed and dynamic confocal microscopy imaging with living markers for centrioles, microtubules, and NuMA on normal and cancer cells after TI exposure to block telomerase activity.

Principal Investigator

Calvin R Simerly, PhD
Research Associate Professor
Magee-Womens Research Institute and Foundation and University of Pittsburgh
204 Craft Avenue B603
Pittsburgh, PA 15213

Other Participating Researchers

Gerald Schatten, PhD – employed by Magee-Womens Research Institute and Foundation and

University of Pittsburgh

Expected Research Outcomes and Benefits

Understanding the dynamics and molecular composition of the cell's spindle poles, centrosomes and spindle assembly checkpoint system in normal and cancerous cells affords new targets for designing chemotherapeutic strategies in oncology. While innovative cancer therapies targeting telomerase with specific inhibitor agents are now undergoing clinical trials, it is of keen importance to understanding the basic biology of these novel drugs and how they impact cell proliferation, growth and division. Understanding the molecular mechanism of telomerase inhibitors on centrosomes and the spindle assembly checkpoint (SAC) constituents may be vital to understanding increasing multipolarity in cancer cells without targeting normal somatic cells, permitting new strategies for the treatment of malignancies. It may also afford a much richer understanding of the link between spindle multipolarity, aneuploidy and malignancy transformation in humans and perhaps give insights into innovative approaches for personalized treatment of cancers.

Summary of Research Completed

The Specific Aims did not change in this reporting period. Excellent progress was made on all questions. We used three main cell lines for this reporting period; CCD-Lu8 normal lung fibroblasts, NCI H292 lung carcinoma, and the MCF7 breast cancer cell line. WI-38 was not investigated due to difficulties in growing and maintaining cells in culture. BIBR (2-[[(2*E*)-3-(2-Naphthalenyl)-1-oxo-2-butenyl1-yl]amino]benzoic acid]1532 remained the telomerase inhibitor employed for our study. We also included two multidrug resistant (MDR) inhibitors, verapamil and tariquidar, since cancer cells reverse the efficiency of compounds *in vitro*. Both MDR drugs, which inhibit the ATP-binding cassette transporters in cancers, have been well documented in the literature and are commercially available. Both MDR inhibitors were prepared in DMSO according to the manufacturer's protocols and kept at -80ºC until use.

Aim 1. What are the effects of Telomerase Inhibitors (TIs) on cancer cell viability, DNA synthesis, metabolic activity, and Telomerase activity?
<u>Question 3. What are the effects of TIs on the metabolic activity of control WI-38 and NCI H292 or MCF7 cancer cells</u>? We investigated BIBR1532 TI effects on the metabolic activity of control versus cancer cell lines with the Vybrant MTT cell proliferation assay kit (Molecular Probes, Eugene, OR), using the quick protocol. A 12mM MTT (3-(4,5-dimethylthiazol-2,5-diphenyltetrazolium bromide) stock solution was prepared according to the manufacture's protocol, briefly spun, and stored at 4°C until use. Control and cancer cells were plated in 96-well plates at a density of 5,000 cells per well and incubated in 0, 75, or 100 µM BIBR1532 for 24 or 72 hrs. Cancer cells, but not the control CCD-Lu8 cell line, were co-incubated with 1µM tariquidar MDR inhibitor. At each time point, 10 microL of the 12mM MTT stock solution was added to each well and incubated at 37ºC for 4 hrs. After MTT labeling, all but 25 µl of the medium in each well was removed, and then 50µl of anhydrous DMSO was added per well, with additional mixing. The samples were then incubated at 37°C in a humidified chamber for 10 minutes, mechanically mixed by pipetting, and the absorbance read at 540 nm on a plate reader. For each time point (24 or 72 hrs), we plotted the 75µM and 100µM BIBR1532-treated cells

against the control (no drug) wells, set to 100% survival. As shown in Figure 1, at 24 hrs post-TI treatment (Fig. 1, left graph), a significant drop in cell proliferation was evident in both NCI H292 and MCF7 cancer cell lines compared to CCD-Lu8 cells within 24 hr of drug application. The slight increase in the NCI H292 cancer line is probably owing to small pipetting errors in performing the quick protocol technique. Interestingly, after 72 hrs of incubation in BIBR1532, the CCD-Lu8 control cells demonstrated a drop in cell viability, especially at 100µM TI exposure (Fig. 1, right graph). This supports our earlier findings that higher concentrations of BIBR1532 TI for periods ≥ 24hr demonstrates unanticipated off-target effects in the CCD-Lu8 control fibroblast cell line. Collectively, these data support our initial hypothesis that the MTT assay would show a significant metabolic activity drop in cancer cells after TI application, with the greatest percentage of metabolic loss at doses ≥50µM and exposure time greater than 24hr. However, higher concentrations of TI do suggest unanticipated drug side effects not related to inhibition of telomerase activity since CCD-Lu8 cells lack telomerase activity (see next question).

Question 4. Do TIs inhibit endogenous telomerase activity in a dose-dependent manner in control WI-38 and NCI H292 or MCF7 cancer cells? To gauge whether BIBR1532 was affecting endogenous telomerase enzyme in cancer cells, we investigated telomerase activity using the TRAPeze telomerase detection kit (Millipore, Temecula, CA). NCI H292 cancer cells were treated with 100 µM BIBR1532, and MCF7 cells were treated with 75 µM BIBR1532, both with 1 µM tariquidar, for 72 hrs. Untreated cancer cells (controls) were incubated in 1 µM tariquidar alone. CCD-Lu8 cells were exposed to 0, 75, and 100 µM BIBR1532 without tariquidar. Both untreated and TI-exposed cells were collected, spun at 700 x g, washed 1x in PBS, and centrifuged again. PBS was removed by a micropipette and the pellets frozen at -80ºC until use. At thaw, samples were suspended in 1x CHAPS lysis buffer and incubated on ice for 30 minutes. Samples were spun in a microcentrifuge at 12,000 x g for 20 min at 4ºC, and a small aliquot of each cell line was used to determine protein concentration, with the concentration adjusted to 100-500 ng/µl. Since telomerase is a heat-sensitive enzyme, a separate aliquot of each treatment was heated to 85ºC to serve as a negative control. All samples were quickly frozen on dry ice and stored at -80ºC until use. Control samples, including the positive telomerase extract control, PCR amplification control, primer-dimer/PCR contamination control, and the telomerase quantitation control template were prepared as described in the manufacturer's instructions. PCR amplification assay was performed as described in the kit instructions and the PCR products run on 10% non-denaturing PAGE gel in 0.5X TBE buffer with appropriate molecular weight size markers at 150 V for 1.5 hrs. Bands were visualized with SYBR Green dye according to the manufacturer's instructions. Telomerase activity was calculated as the intensity ratio of the 36-bp standard to the ladder bands, with the percentage of inhibition calculated by comparing telomerase activity of control versus BIBR1532-treated cells. As shown in Figure 2 (graph), both cancer cell lines showed significant reduction (~70%) in endogenous telomerase activity as measured by the TRAPeze assay when compared to tariquidar-treated control cancer lines. No telomerase enzymatic activity was identified in the control CCD-Lu8 lung fibroblast line. A representative gel run is shown in Figure 2, right panel. Of importance, this technique was performed multiple times since false-negative results frequently occur. This was particularily evident when samples had excessively high telomerase activity and the 36-bp band was not visible, perhaps owing to amplification of the TRAP products and 36-bp band being semi-competitive. Only when runs met all conditions for a valid assay (36-bp internal control band

only in the CHAPS buffer lane; the telomerase-positive control lane showing both the 36-bp internal control band and ladder products with 6-base increments starting at 50-bp; and heat-treated samples with no ladder and only the 36-bp internal control band visible) could the assay be utilized to analyze our cell extracts. We were successful in two runs, as shown in Figure 2 (graph). Taking this all together, we demonstrated that BIBR1532 TI caused significant reductions in telomerase activity in our tested cancer, but not control, cell lines.

Aim 2. At the maximum effective dose of TIs which inhibits cell growth and proliferation of cancer cells as determined in Aim 1, what are the impacts of telomerase inhibition on centrosome and centromere function in control WI-38 and NCI H292 or MCF7 cancer cells?
Question 1. Do TIs impact microtubule (mt) organization from the centrosome and do they affect mt dynamics following drug induced disassembly or rescue from mt depolymerization? We exposed control and cancer cell lines to either 1µM tariquidar or 100µM BIBR1532 with 1µM tariquidar for 48 hrs. Mts were then disassembled by treatment for 1 hr at 37ºC with 10µM nocodazole and then either fixed in methanol (no recovery) or permitted to recover in normal culture media for 15 min prior to methanol fixation (rescued). Each sample was immunostained for a centriole marker (CEP 135; Millipore), mts (YOL 1/34; Millipore), and Hoechst DNA (Sigma-Aldrich, St. Louis, MO). Fixation times, immunostaining, and image capture parameters (focal depth, laser settings, image box size, and region of interest) were exactly the same for each cell line and all four treatments. A region of interest (ROI) was drawn around each interphase centriole to include mts, the same ROI being used for each fixed sample. The pixel intensity within each ROI was determined using Elements software (n=>6) and average intensity analyzed over three independent trials. The pixel intensity in the rescued cell lines were compared to the pixel intensity of non-recovered cell lines for each treatment and graphed. As shown in Figure 3, TI with tariquidar did not impact mt recovery in CCD-Lu8 cells that lack telomerase activity (left graph) but did significantly impact mt recovery in both NCI H292 (middle graph) and MCF7 cells (right graph). Collectively, these data suggest that BIBR1532 impacts mt regrowth from the centrosome at interphase, following rescue from mt disassembly with nocodazole, in cancer cells relative to control cells. Since high-TI concentrations block cell cycle progression in cancer cells, we could not determine the effects on mitotic events.

Question 2. Do TIs block centrosome duplication in a dose-dependent manner? We utilized stably transduced GFP centrin-tagged CCD-Lu8, NCI H292, and MCF7 cell lines to dynamically image centrioles in the absence or presence of BIBR 1532 and tariquidar by time-lapse video microscopy (TLVM). GFP centrin-tagged cell lines were plated onto sterile 35-mm Matek glass bottom petri dishes and imaged on a Nikon Eclipse T_i inverted microscope equipped with Perfect Focus to prevent Z-axis drifting during prolonged live-imaging. A high-resolution objective (Plan Fluor oil x100 objective [NA=1.3]) was utilized to capture images using an Andor CCD camera and Nikon Elements software. Cells were maintained at 37ºC and 5% CO_2 using a Tokai stage top incubator. As shown in Figure 4 for MCF7 cancer cells, exposure to 1µM tariquidar for 48 hrs did not interfere with assembly of a bipolar spindle, with centrioles located at each spindle pole, (Fig. 4A-D) that ultimately underwent normal cell division. However, simultaneous exposure to 75µM BIBR1532 and 1µM tariquidar for 48 hrs severely slowed cell cycle progression, and rarely were mitotic MCF7 cells observed. In two imaging sessions, MCF7 cells exposed to BIBR1532 and tariquidar were observed to round up, transition into mitosis, and undergo nuclear envelope breakdown. As shown in Figures 4E-H, a single centriole in the

cytoplasm did not duplicate or split at mitotic onset and this cell did not divide after 9 hrs. The exposure of MCF7 cells to TI and tariquidar was reversible after 48 hrs rescue in normal culture medium (Fig. 4I-L). Rescue cells entered mitosis, assembled a bipolar spindle with centrioles at each spindle pole and divided within 1 hr of TLVM. For GFP centrin-tagged NCI H292 cells, no cells exposed to 75 µM BIBR1532 and 1 µM tariquidar entered into mitosis (n=5; data not shown). Taken together, we demonstrated abnormal centriole behavior in live MCF7cancer cells following BIBR1532 treatment. Centrioles did not duplicate, as only a single centriole was observed in the cytoplasm. Mitosis was rarely detected after high TI and did not proceed normally, displaying abnormal mitotic spindle assembly, mis-segregated centrosomes, and failure to complete cell division.

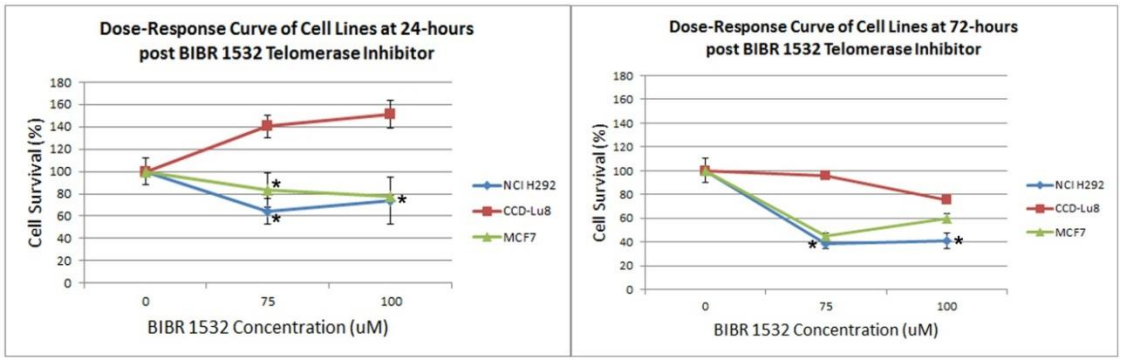

Figure 1. Analysis of BIBR1532 effects on metabolic activity of control and cancer cells as measured by the MTT assay. Control and cancer cells were treated with the designated concentrations of BIBR1532 for 24 or 72 hrs prior to MTT assay analysis. NCI H292 and MCF7, but not CCD-Lu8, were simultaneously treated with 1µM tariquidar. We plotted the percentage of cell survival against the inhibitory effect of BIBR1532 concentration after 24 or 72 hrs. Values are mean ± SD of three independent experiments. ∗: $p < .05$, significant changes from CCD-Lu8 control cells (red line).

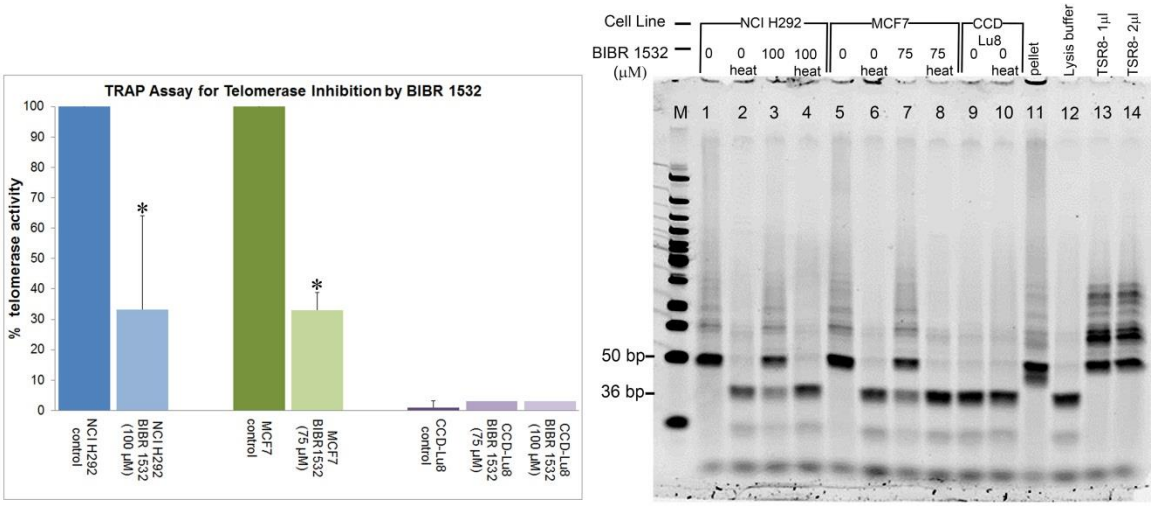

Figure 2. T*elomerase enzymatic activity inhibition by BIBR1532 in control and cancer cell lines*. NCI H292 cells treated with 100µM BIBR1532, MCF7 cells with 75µM, and CCD-Lu8 with both 75µM and 100µM. 1µM tariquidar was included in cancer cell lines. After 72 hr, telomerase activity (TA) was determined using the PCR-based TRAPeze assay resolved on 10% PAGE with Sybr Green band detection. TA was calculated using the intensity ratio between the 36-bp standard and ladder bands, with the percentage of inhibition calculated by comparing TA of control versus BIBR1532-treated cells. Left graph: Telomerase activity is significantly reduced in both NCI H292 and MCF7 cancer cells, but not in the control CCD-Lu8 fibroblast line, that lacks telomerase enzyme. Values are given as mean ± standard error of two independent experiments. *: $p<0.05$ significance from control lines. Right gel: TRAP pcr 10% PAGE gel showing 36-bp band and telomerase ladder in NCI H292 lung carcinoma (lanes 1-4), MCF7 breast cancer (lanes 5-8), CCD-Lu8 control lung fibroblasts (lanes 9 and 10), and standard controls (lanes 11-14). Here, the 36-bp band is absent in five samples owing to high telomerase activity (i.e., lanes 1, 5, 11, 13, 14).

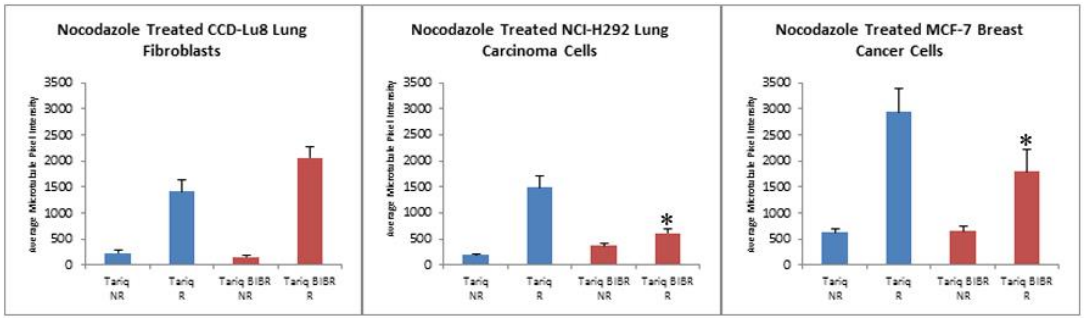

Figure 3. Microtubule recovery dynamics after 10µM nocodazole treatment in CCD-Lu8 control, NCI H292 lung carcinoma, and MCF7 breast cancer cells following exposure to BIBR1532 and tariquidar. Cell lines were treated for 48hrs in either 1µM tariquidar alone (blue bars) or combined 100µM BIBR1532 and 1µM tariquidar (red bars) followed by 1 hr incubation in 10µM nocodazole in the presence of the drugs. Cell lines were then either fixed in absolute methanol (NR: no rescue) or permitted a 15 min recovery in normal culture medium (R: rescue) prior to methanol fixation. The average microtubule pixel intensity was measured in interphase cells, after drawing a region of interest around the centrioles with Elements software, and plotted. Pixel intensity in the rescued cell lines was compared to the pixel intensity of non-recovered cell lines for each treatment. *: p value < 0.05 represents significant difference from the tariquidar control values, indicating lower overall microtubule recovery.

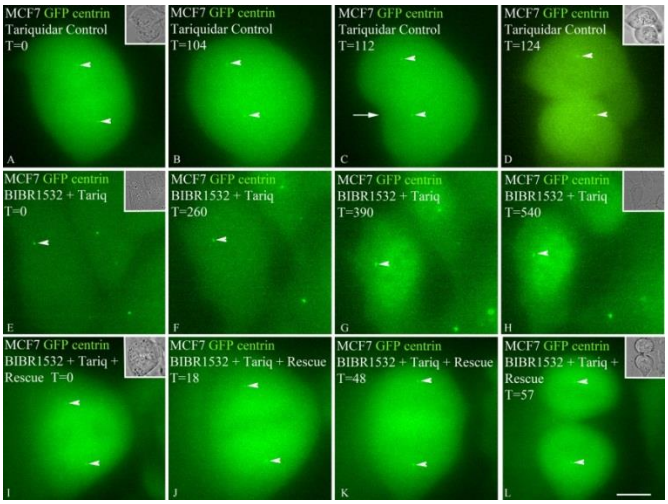

Figure 4. Time-lapse video microscopy of GFP-centrin tagged MCF7 cells in the presence of the telomerase inhibitor BIBR1532 for 48 hrs. A-D: GFP-centrin MCF7 cells imaged in 1µM tariquidar multidrug resistance inhibitor, showing bipolar spindle assembly with centrioles at each spindle pole (arrowheads) and ultimate cell division within 2 hrs post imaging (D: inset, brightfield). E-H: GFP centrin tagged MCF7 cells imaged in the presence of 1µM tariquidar with 75µM BIBR1532 for 9hrs. Although this cell appeared to round up and enter into mitosis, the centrosomes never duplicated or separated at the beginning of mitosis (G: arrowhead) and failed to progress through mitosis or cell division (H: inset, brightfield). I-L: GFP-centrin MCF7 cells were treated with tariquidar + BIBR1532 for 48 hrs and allowed to recover for 48hrs in normal culture medium before imaging. Note: a bipolar spindle is assembled with duplicated split centrioles (I: arrowheads), with normal cell division occurring by 57 min post imaging (L: inset, brightfield). Image times are shown in each panel. Arrowheads depict GFP-tagged centrioles. Insets in A, E, and I are brightfield pre-imaging of cells. Insets in D, H, and L are brightfield images post image acquisition. Bar= 5µm.

Research Project 6: Project Title and Purpose

Genetic Biomarkers of Inherited and Acquired Forms of Male and Female Germ-cell Infertility – We propose a novel pilot study to investigate genome-wide DNA coding mutations related to male and female infertility using novel oligonucleotide microarray Comparative Genome Hybridization (CGH) and Next Generation Sequencing. We expect to identify a significant number of genomic, genetic, inherited and de-novo germ-cell-specific defects characteristic for infertile male and female germ cells (sperm and oocyte). We hypothesize that these findings will highlight disruption(s) of specific molecular mechanisms of spermatogenesis and oogenesis and would serve as future infertility-associated diagnostic markers of pathological reproductive tissues.

Duration of Project

1/1/2013 – 12/31/2013

Project Overview

Infertility is defined as the reproductive failure or inability of a couple to conceive in one year. Commonly, male factor etiology is associated with semen deficiencies and female infertility relates to various oocyte defects. Among the most common semen abnormalities observed in infertile males are azoospermia (AZ, absence of male germ cells in semen) and oligozoospermia (OS, low sperm concentration) accounting for ~50% of all cases. The most common ovarian pathologies are polycystic ovarian syndrome, premature ovarian insufficiency/failure,

amenorrhea, and ovulatory disorders (reduced or absent ovulation). At least 30% of infertile couples are diagnosed with unknown etiology (aka idiopathic male or female infertility). This reflects our poor understanding of the underlying pathological molecular mechanisms in spermatogenesis, oogenesis, and fertilization. To date, only a small proportion of infertile men and women are diagnosed with definitive genetic defects, while the vast majority of patients have descriptive clinical diagnosis without a known cause and have no medical cure. We propose a pilot genome-wide study to investigate genomic mutations using novel oligonucleotide micro array Comparative Genome Hybridization (aCGH) and Next Generation Sequencing. We anticipate identifying genomic and genetic germ-cell defects characteristic for infertile male and female germ cells (sperm and oocyte). We hypothesize that we will detect a significant number of genomic aberrations, DNA mutations that disrupt vital molecular mechanisms in spermatogenesis and oogenesis that would serve as future biomarkers of infertility. Identification of specific gene defects associated with infertility will help with the future development of novel diagnostic procedures in infertile couples. This research will serve as proof of principle of our abilities to generate and analyze enormous genomic data sets of aCGH and Whole Exome Sequencing technologies.

Specific Aim 1. Identify infertility-associated genomic aberrations using oligonucleotide aCGH.
Specific Aim 2. Genome-wide screen for infertility-associated mutations and candidate genes by Next Generation DNA Sequencing (Whole Exome Sequencing).

Principal Investigator

Alexander Yatsenko, MD, PhD
Visiting Assistant Professor
Magee-Womens Research Institute and Foundation and University of Pittsburgh
204 Craft Avenue
Pittsburgh, PA 15213

Other Participating Researchers

Michelle Zorilla, MS – employed by Magee-Womens Research Institute and Foundation

Expected Research Outcomes and Benefits

Infertility is a global health problem that affects 10-15% of American couples. Yet a majority of infertile males receive descriptive diagnosis. Widely used to help infertile couples, assisted reproductive technologies while helping many couples, could introduce underlying genetic causes of infertility to assisted offspring. Thus, it is essential to better understand the underlying genetic etiologies of male and female infertility both for the diagnosis and treatment of the infertile males and females as well as for appropriate genetic counseling. Despite a wealth of evidence from animal models that many autosomal genes could contribute to male and female reproductive defects, current genetic testing is limited. There are karyotype and Y microdeletion and fragile X chromosome analyses used for men and women with clinical descriptive and idiopathic infertility. We propose to apply highly efficient genomic approaches, such as genome-wide microarray CGH analysis of genomic imbalances, and high throughput exome sequencing

of all known genes, to comprehensively examine genetic contribution to germ-line infertility and detect mutations with highest outcome available. We have partnered with an internationally renowned Reproductive Endocrinology and Andrology Clinic at Magee Womens Hospital UPMC, to enroll and design a compelling approach to accomplish our aims. This research aims to generate new information that will advance clinical genetic testing and counseling for the infertile couples. We hypothesize that our efforts will generate preliminary information that can be utilized in the future diagnostic genetic testing in couples with infertility. Moreover, our studies are likely to discover novel biologic markers of human male and female reproduction.

Summary of Research Completed

Specific Aim 1. *Identify infertility-associated genomic aberrations in AZ and POI patients using oligonucleotide microarray Comparative Genome Hybridization (aCGH) technology.*

During this period, we finished CGH analysis for 10 infertile men with azoospermia and 10 infertile men with normozoospermia. We isolated DNA from white blood cells and assessed the DNA's quality and amount; DNA samples with suboptimal quality were subjected to DNA purification via purification columns (Puregene). We performed a genome-wide study of genomic abnormalities via high-resolution genome-wide 400K CGH microarray (Agilent).

DNA fragmentation and Cy5 labeling were performed with 1 μg of high-quality patient DNA. An equal amount of sex specific control DNA (Promega) was fragmented and Cy3 labeled, following the same protocol. The hybridization procedure was completed according to the Agilent protocol. Microarray results were obtained via Agilent SureScan microarray D scanner. The quality of the microarray results was assessed by standard QC report values: dye signal intensities, background noise, and ratio of signal to background noise. If these values were outside high-quality range, we repeated the experiment.

The CGH data were screened for aberrations by CytoGenomics' default Aberration Detection Method 2. The algorithm identifies statistically significant copy number variations (CNVs) by determining the consistency of the log ratio across all probes in the aberration. The quality of the probe log ratio, based on its signal-to-noise ratio, is also factored into the significance score. Aberrations were also required to have at least three probes in the CNV region, as well as a minimum absolute log ratio of plus or minus 0.25 in the region of interest. We identified between 18 and 51 CNVs per patient, with an average of 43 CNVs and aberration sizes ranging from 40 kilobases (Kb) to 3 megabases (Mb). Current results of our genome-wide CGH study for two selected patients are shown in Table 1. In these patients, we identified three CNV regions with deletions in highly plausible candidate genes for male infertility (Fig. 1). One patient had a small, nearly 12 Kb internal deletion in the gene *SBF1*on chromosome 22. *SBF1* encodes a testis-specific psuedophosphatase. The other patient had a small E deletion that removed a portion of the gene *RIF1* on chromosome 2 *RIF1*encodes homeobox transcription factor, a protein involved in mitotic division. Previously, knock-out models of these genes in male mice were shown to cause spermatogenesis defects, azoospermia, and infertility.

Further study of deletion break point in first candidate, X-linked *TEX11* using an X-chromosome CGH array (Fig. 2**)**, long range PCR (Fig. 3), and quantitative polymerase chain reaction (qPCR)

(Fig. 4) confirmed our finding.

Specific Aim 2. *Identify infertility-associated mutations and candidate genes by a genome-wide screen with Next Generation DNA Sequencing (Whole Exome Sequencing, WES).*

During this period, we studied DNA samples from Family no. 2, with azoospermia, including one infertile male patient, one fertile brother, and their parents. We amplified DNA, hybridized it with Capture Library and ran WES for the family. Their bioinformatic and sequencing analysis is in progress.

We performed a standard human exome capture procedure using Agilent exome capture library V4.2 + UTRs, which covers 71 Mb of coding and flanking sequences and enriches coding regions. WES was run on a HISeq2000 machine (Illumina). Sanger sequencing was used to confirm positive WES findings. Bioinformatic analysis was performed with open access and commercial NextGENe software (SoftGenetics). To test for small genomic aberrations and for homozygosity, we ran the 400K CGH (Agilent) and 700K SNP (Illumina) arrays, respectively. From each family member, we obtained on average ~6.0 Gb of sequencing results. The average exome coverage was 62X. Nearly 94% of the targeted exome sequence had 10X coverage or higher, with Phred-like consensus quality of 30. Furthermore, Phred quality >9 (chance of error = 0.001) was used to remove sequencing run errors.

In Family 2, we ran sequencing, raw read alignment to the reference genome (hg19) and preliminary sequencing analysis of the family members, using the previous bioinformatic pipeline. We identified ~57,000 single-nucleotide polymorphisms (SNPs) and indels. For Family 2, we applied two models of autosomal recessive and X-linked inheritance of azoospermic defects. In this family, we had an unaffected brother, which allowed us to remove all shared variants between brothers, leaving 8,437 homozygous mutations and 8,823 compound heterozygotes.

Using bioinformatic filtering for autosomal recessive and X-linked inheritance models, we retained 1,259 homozygous and 2,140 compound heterozygous non-synonymous variants in exons or flanking intronic regions. These variants were filtered against known SNPs in the dbSNP135 database and SNPs with population frequency >1% were excluded, leaving 411 novel variants.

Further filtering, using male reproductive tissue-specific expression and protein function, led to a total of nine novel homozygous, compound heterozygous, and hemizygous sequence variants. From these candidate genes, our preliminary analysis indicated seven azoospermia candidate genes likely to have deleterious effects. These results could be interpreted as single gene disorder, polygenic disease, and complex genetic disorder.
Since identified genes mutations can be explained by different modes of inheritance, we are currently designing multiple functional studies that are necessary to provide evidence that specific mutation(s) have deleterious effect on sperm function. These include creation of *in vivo* mouse knock-out models and *in vitro* functional assays. These studies are out of scope for this project and will be funded and performed under future State and/or Federal funding agencies.

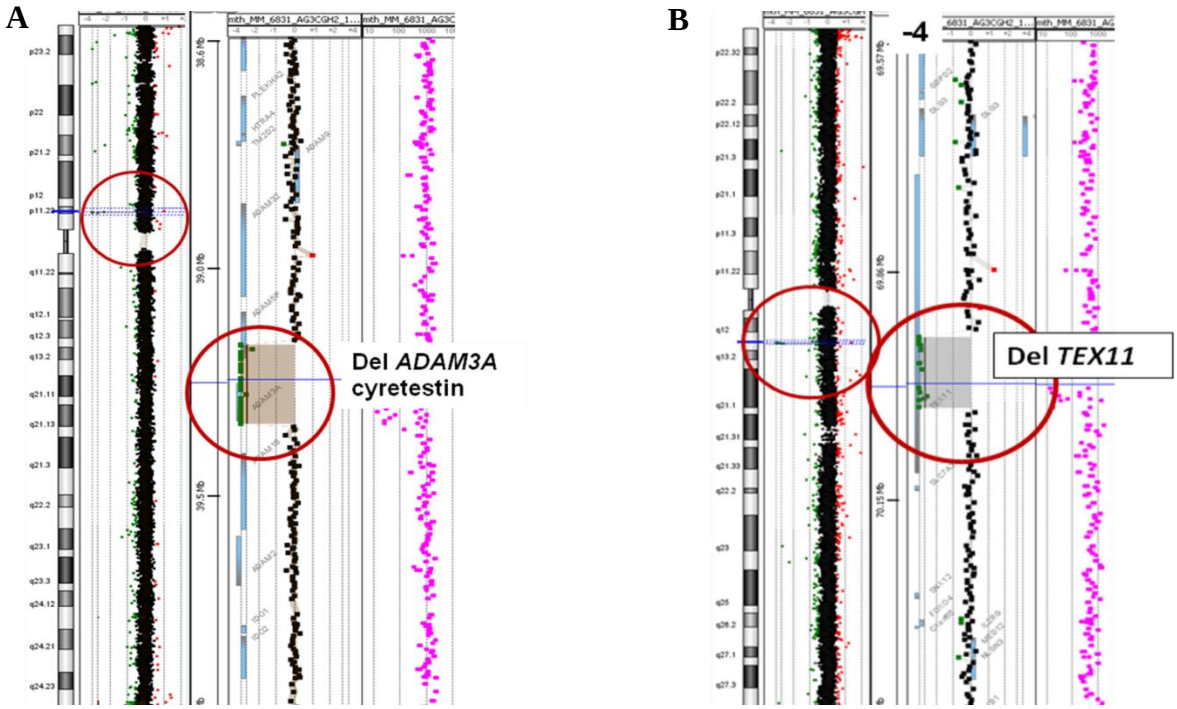

Figure 1. CGH analysis for two selected azoospermic patients with male infertility. **A.** Homozygous ~50Kb deletion that removes more than half of ADAM3A gene. **B.** Nearly 90Kb deletion of the Tex11 X-linked gene affects three coding exons of the gene.

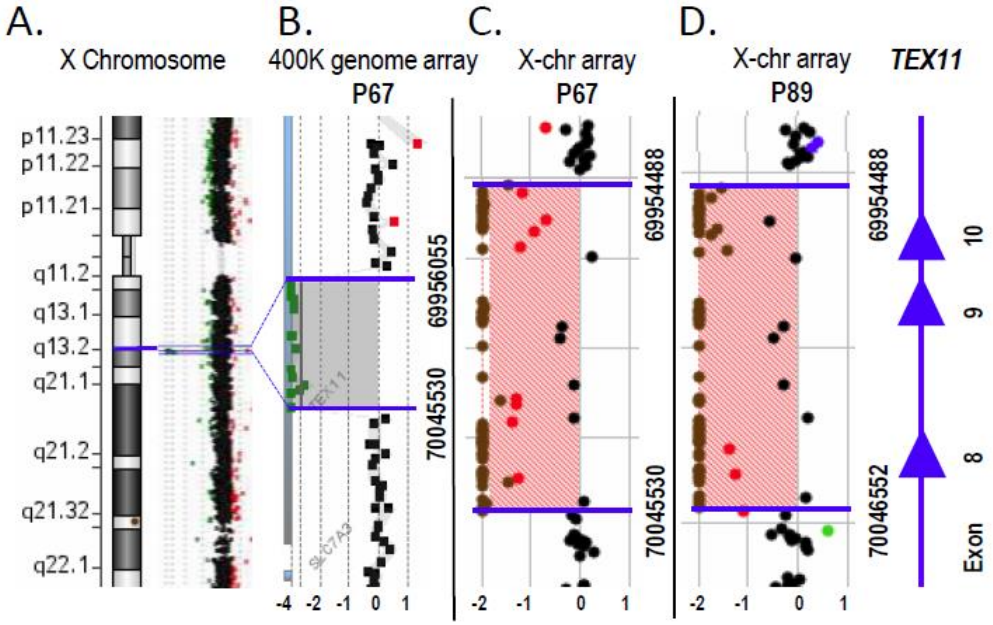

Figure 2. Hemizygous deletion of *TEX11* exons 8-10 and flanking intronic regions in two azoospermic males. **A.** Comparative genomic hybridization (CGH) with ~400K array, showing a deletion on the X13.2 region of the X chromosome, highlighted in blue. **B.** The deletion includes 12 probes in the gene *TEX11*, spanning about 90 Kb. **C, D.** A custom X chromosome array with ~180K probes further defined the deletion to 91,042 (**C,** P67) and 92,064 bp (**D,** P89), encompassing exons 8-10. In sample P67, the deletion covers chromosome X: 69,954,488-70,045,530 (hg19), and in P89, the deletion covers chrX:69,954,488-70,046,552 (hg19).

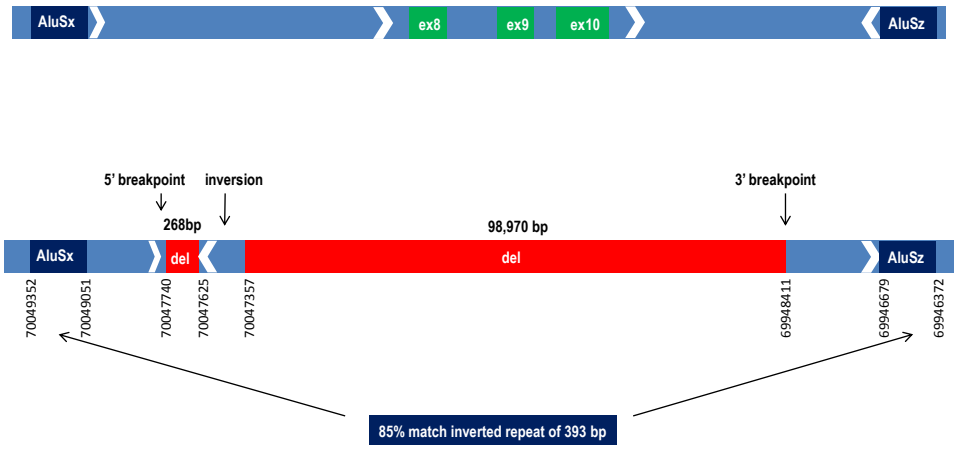

Figure 3. Genomic structure of the *TEX11* deleted region defined by long-range PCR and sequence analysis. The deletion covering exons 8-10 is shown in red. Alu repeats are shown in dark blue. Green boxes, ex8, ex9, and ex10, abbreviate *TEX11* exons 8-10. 5' and 3' breakpoints and genomic coordinates are displayed above and below the diagram.

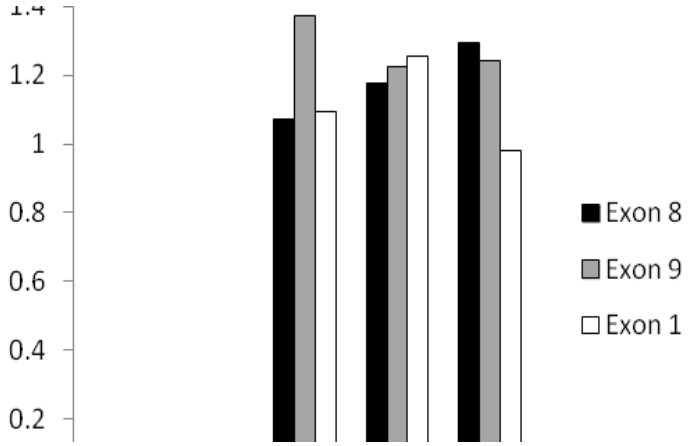

Figure 4. qPCR analysis of deletion exons 8-10 of *TEX11*. Fold change of four azoospermic samples and Promega male control, calculated by delta Ct, with Actin beta serving as an internal control. P67 and P89 show a fold change of ~0, with no amplification of *TEX11* exons 8-10. Azoospermic samples P1 and P46 and normal Promega male DNA serving as controls, display a fold change of 1.19 +/- 0.12. Exon 8 is represented by a black bar, exon 9 by a grey bar, and exon 10 by a white bar.

Table 1. Summary of array Comparative Genome Hybridization (CGH) findings for two selected patients. Copy Number Variants (CNVs) with loss of DNA are shown in green, and regions with amplification are shown in red. Amp/Del is amplification (gain) and Del is deletion (loss).

Event No	Chromosome	Cytoband	#Probes	Amp/Del	P-value	Annotations
	Patient 1					
1	chr1:1651368-1664221	p36.33	3	-0.883733	N	CDK11B, CDK11A,
2	chr1:149041933-149378266	q21.2	25	-0.749372	N	LOC388692, FCGR1C
3	chr1:152556449-152586281	q21.3	7	1.250532	N	LCE3C
4	chr1:169206875-169241333	q24.2	7	0.650861	N	NME7
5	chr1:196742735-196796220	q31.3	5	-4.391853	N	CFHR3, CFHR1
6	chr2:34697718-34730142	p22.3	7	-0.623769	N	
7	chr2:133023456-133690492	q21.2	118	0.511247	N	GPR39, LYPD1, NCKAP5
8	chr2:186043764-186094608	q32.1	4	-1.010610	N	
9	chr3:89394229-89416802	p11.1	5	-0.873299	N	EPHA3
10	chr3:195354124-195456540	q29	13	0.911784	N	SDHAP2, MIR570,
11	chr4:69387056-69483277	q13.2	12	-0.611766	N	UGT2B17, UGT2B15
12	chr4:70156093-70259782	q13.2	4	-0.711528	N	UGT2B28
13	chr5:140223256-140236399	q31.3	4	-0.899342	N	PCDHA1, PCDHA2,
14	chr5:150204997-150221011	q33.1	4	-0.897815	N	
15	chr5:155471484-155488272	q33.2	4	0.696758	N	
16	chr6:32455274-32521929	p21.32	10	-1.260594	N	HLA-DRB5, HLA-DRB6
17	chr6:78979172-79023328	q14.1	4	0.737965	N	
18	chr7:53461023-53583184	p12.1	13	-0.925909	N	
19	chr7:64691376-65308719	q11.21	63	0.578799	N	INTS4L1, ZNF92,
20	chr7:133788914-133797387	q33	3	-2.960330	N	
21	chr7:152456633-152459393	q36.1	3	0.956476	N	ACTR3B
22	chr8:39234992-39243892	p11.22	2	-4.759742	N	ADAM5P
23	chr8:39243952-39299581	p11.22	10	-4.339831	N	ADAM5P
24	chr8:39299582-39322744	p11.22	6	-5.269302	N	**ADAM3A**
25	chr8:39322745-39386158	p11.22	10	-4.339831	N	**ADAM3A**
26	chr8:144990160-145021210	q24.3	12	0.510021	N	PLEC1, MIR661
27	chr9:43505843-43836428	p12 - p11.2	6	0.579641	N	FAM75A6
28	chr9:139407170-139419558	q34.3	4	0.805466	N	NOTCH1
29	chr10:56448627-56468820	q21.1	5	1.062546	N	PCDH15
30	chr11:55372753-55450788	q11	15	-0.373397	N	OR4P4, OR4S2, OR4C6
31	chr12:9637323-9718846	p13.31	11	1.554651	N	
32	chr12:11221333-11249210	p13.2	5	0.678460	N	PRR4, PRH1, TAS2R43
33	chr14:19376762-20420849	q11.2	35	0.525080	N	OR11H12, POTEG,
34	chr14:74001651-74012568	q24.3	3	-2.737513	N	HEATR4, ACOT1
35	chr15:20432851-22578630	q11.1 - q11.2	99	-0.532005	N	GOLGA6L6, GOLGA8C,
36	chr15:34727647-34795913	q14	12	-0.944041	N	GOLGA8A
37	chr15:102394651-102480888	q26.3	6	-0.671294	N	OR4F4
38	chr17:34437475-34475514	q12	7	0.510489	N	
39	chr17:44171888-44351152	q21.31	25	0.553454	N	KIAA1267
40	chr19:20628487-20701620	p12	7	-0.771655	N	
41	chr20:1563715-1584485	p13	6	-1.888616	N	SIRPB1
42	chr22:16133474-17340318	q11.1	36	-0.850754	N	POTEH, OR11H1,
43	chr22:42907787-42945064	q13.2	5	0.903594	N	SERHL, RRP7A
44	chrX:159430-216099	p22.33	21	0.424186	N	PLCXD1
45	chrY:109430-166099	p11.32	21	0.424186	N	PLCXD1

	Patient 2					
1	chr1:152556449-152581944	q21.3	6	-1.809761	N	LCE3C
2	chr2:34702930-34730142	p22.3	6	-0.641106	N	
3	chr3:162514534-162619141	q26.1	10	0.737044	N	
4	chr4:69387056-69483277	q13.2	12	-4.424659	N	UGT2B17, UGT2B15
5	chr4:186401069-186419493	q35.1	4	-0.972009	N	
6	chr6:32455274-32527058	p21.32	11	0.729228	N	HLA-DRB5, HLA-DRB6
7	chr6:78979172-79023328	q14.1	4	0.754265	N	
8	chr8:7169490-7786708	p23.1	10	0.447477	N	FAM66B, DEFB109P1B,
9	chr10:132360482-132370482	q26.3	3	0.894809	N	
10	chr11:55368154-55438473	q11	14	0.615986	N	OR4C11, OR4P4, OR4S2...
11	chr12:9637323-9718846	p13.31	11	0.854927	N	
12	chr12:11225616-11249210	p13.2	4	-3.337609	N	PRR4, PRH1, TAS2R43
13	chr14:19728641-20420849	q11.2	31	-0.707113	N	P704P, OR4Q3, OR4M1...
14	chr14:106531557-106559103	q32.33	7	-3.656430	N	
15	chr14:106785927-106810907	q32.33	3	0.995461	N	
16	chr14:106875948-106931193	q32.33	12	-0.692606	N	
17	chr15:20481702-22578630	q11.1 - q11.2	98	0.304351	N	GOLGA6L6, GOLGA8C,
18	chr16:21475039-21593631	p12.2	6	-0.996479	N	LOC100271836,
19	chr20:1563715-1584485	p13	6	-2.632721	N	SIRPB1
20	chr22:24347959-24395353	q11.23	10	-3.789411	N	LOC391322, GSTT1,
21	chr22:39359112-39385485	q13.1	6	-0.966253	N	APOBEC3A, APOBEC3B
22	chrX:61091-70396	p22.33	2	0.355181	N	
23	chrX:70397-92387	p22.33	6	1.028388	N	
24	chrX:92388-339035	p22.33	55	0.355181	N	PLCXD1, GTPBP6,
25	chrX:69956055-70045530	q13.1	14	-3.932159	N	TEX11
26	chrY:11091-20396	p11.32	2	0.355181	N	
27	chrY:20397-42387	p11.32	6	1.028388	N	
28	chrY:42388-289035	p11.32	55	0.355181	N	PLCXD1,